Probing Energy Landscapes of Cytochrome b_6f with Spectral Hole Burning: Effects of Deuterated Solvent and Detergent

Alexander Levenberg

A Thesis
In
The Department
of
Physics

Presented in Partial Fulfillment of the Requirements
for the Degree of Master of Science (Physics) at
Concordia University
Montreal, Quebec, Canada

April 2018

CONCORDIA UNIVERSITY

School of Graduate Studies

This is to certify that the thesis prepared

By: Alexander Levenberg

Entitled: Probing Energy Landscapes of Cytochrome b_6f with Spectral Hole Burning: Effects of Deuterated Solvent and Detergent

and submitted in partial fulfillment of the requirements for the degree of

Master of Physics

complies with the regulations of this University and meets the accepted standards with respect to originality and quality.

Signed by the final examining committee:

Dr. Mariana Frank _____ Chair

Dr. Laszlo Kalman _____ Examiner

Dr. Christophe Grova _____ Examiner

Dr. Valter Zazubovits _____ Supervisor

Approved _____

Chair of Department or Graduate Program Director

_____ 2018 _____

André Roy

Dean Faculty of Arts and Sciences

ABSTRACT

Probing Energy Landscapes of Cytochrome b_6f with Spectral Hole Burning:

Effects of Deuterated Solvent and Detergent

Alexander Levenberg

Proteins are complex organic compounds that are among the fundamental molecules of biology. They are the building blocks of life on Earth, responsible for most of the complex functions, evolving and adjusting themselves for millions of years of changing condition of the environment. For the last century scientists all around the world are trying to crack down the mystery of protein folding, its structure, sequences, and conformational changes.[1] The advances in different research techniques have uncovered the interplay of these hidden features in many areas, yet we are far away of complete understanding of the functioning of the proteins. Even if today's methods are capable of providing us with the crystal structure or decipher the amino acid sequence of the protein, the conformational changes affecting the functionality need to be studied further. In order to reveal some parts of this mystery we carry out our research performing Spectral Hole Burning to study protein dynamics. Unfortunately protein does not absorb in the visible range, forcing one to use a dye marker or to pick a protein that naturally has

a marker. Presently pigment-protein complexes of photosynthesis process have become a natural choice for such studies, providing necessary information to study the conformational changes associated with light absorption. In this study we focus on Non-Photochemical Spectral Hole Burning (NPHB) and spectral hole recovery experiments on cytochrome b_6f protein This protein exhibits behavior that is almost independent of the deuteration of the buffer / glycerol glassy matrix containing the protein, apart from some differences in heat dissipation. On the other hand, strong dependence of the hole burning properties on sample preparation procedures was observed and attributed to a large increase of the electron-phonon coupling and shortening of the excited-state lifetime occurring when *n*-dodecyl β-D-maltoside (DM) is used as a detergent instead of n-octyl β-D-glucopiranoside (OGP). The data was analyzed assuming that the tunneling parameter distribution or barrier distribution probed by NPHB and encoded into the spectral holes contains contributions from two non-identical components with accidentally degenerate excited state tunneling parameter (hole burning yield) distributions. Both components likely reflect protein dynamics, although with some small probability one of them (with larger mass of the tunneling entity or the displacement along the generalized coordinate) may still represent the dynamics involving specifically the –OH groups of the water / glycerol solvent. Single proton tunneling in the water / glycerol solvent environment or in the protein can be safely excluded as the origin of observed NPHB and hole recovery dynamics. The illumination intensity dependence of the hole growth kinetics in deuterated samples likely reflects differences in heat dissipation between protonated and deuterated samples. These differences are most probably due to the higher interface thermal resistivity between (still protonated) protein and deuterated water / glycerol outside environment.

Acknowledgements

Foremost, I would like to express my sincere gratitude to my supervisor Dr. Valter Zazubovits, his office door in both the virtual and the real world have always been open to me, whenever I ran into a trouble spot or had a question about my research or writing. He consistently allowed this paper to be my own work, but steered me in the right directions so many times whenever I needed it, keeping himself patient and supportive.

Besides my supervisor, I would also like to thank Dr. Laszlo Kalman for his willingness to help and for his elucidating questions that helped to place the body of research in multimodal perspective**.** I would also like to express my gratitude to Dr. Christophe Grova, I am indebted to him for his comments on this thesis and the defense. I am also extremely grateful to all my committee members for their assistance and time.

Thanks for all my fellow graduate students for making the pleasant working atmosphere and for the midnight scientific debates at physics department at Concordia.

Last, but not the least, I would thanks my family for being supportive, kind and understanding. I must express my very profound gratitude to my wife for providing me with unfailing support and continuous encouragement throughout my years of study and through the process of researching and writing this thesis. This accomplishment would not have been possible without them.

Thank you.

Contents

List of Figures

Abbreviations

Car	Carotenoid
Chl	Chlorophyll
Cyt	Cytochrome
EET	Excitation Energy Transfer
ETC	Electron Transfer Chain
HB	Hole Burning
HGK	Hole Growth Kinetics
FLN	Fluorescence Line Narrowing
PEL	Protein energy landscape
NPHB	Non-Photochemical Hole Burning
PHB	Photochemical Hole Burning
PSI	Photosystem I
PSII	Photosystem II

PSBH Phonon Side Band Hole

RC Reaction Center

SD Spectral Diffusion

SDF Site Destribution Function

SHB Spectral Hole Burning

SSA Single Site Absorption

TLS Two Level System

ZPH Zero Phonon Hole

ZPL Zero Phonon Line

Chapter 1

Introduction

Proteins are complex organic polymer molecules that carry out many different functions in living organisms. *In vivo* the proteins are folded into tertiary and, in some cases into quaternary structure providing the desirable functionality. The folding of proteins is a complicated process that must be guided by some rules in order to avoid the Levinthal's paradox of random folding which predicts astronomical number of possible conformations; therefore to attain the right conformation by sequential probing all the possible conformations would require approximately the lifetime of the universe. Couple of theories were proposed to explain reasonably fast folding occurring in real life [2]. In any case, by the end of the process the protein always reaches its native state, or in a more comprehensive picture, a number of energetically close native substates. The fluctuations between these states may be understood using the concept of the protein Energy Landscape, a concept proposed by Joseph Bryngelson and Peter Wolynes. [99] The conformational changes have a direct impact on the function of a protein. These functions of proteins depend on a large variety of factors such a surrounding solvent, pH, coenzyms etc. All of these lead to protein structure fluctuation in its tertiary structure that in turn may lead to conformation change. Nowadays there are a lot of techniques that are capable of shedding light on protein structure, for example secondary structure maybe determined by circular dichroism

method or tertiary structure by X-ray crystallography, Nuclear Magnetic Resonance spectroscopy or bioinformatics. These methods provide only partial information not sufficient to study the dynamics of the protein. To study the dynamics one may employ optical measurements. However, proteins do not absorb in the visible region, hence some marker must be embedded into the structure. That can lead to structural, conformational change, therefore dynamics of such proteins with artificially embedded dyes may be not correct. Other approach is to choose some protein that has a naturally embedded pigment. Protein-pigment complexes involved in photosynthesis process are outstanding candidates for this research due to their strong absorbance in visible region and natural abundance. The chlorophyll is intrinsic or natural fluorophore, which provides a possibility to study these pigment-protein complexes of photosynthesis while all the stricture of the complex is conserved in its natural state. Moreover, one can be sure that illuminating the sample by the light of visible spectra would not cause any weird, not natural reaction or conformational change.

As it was mentioned above, a protein in general is a complex molecule or a complex of several subunits that has very well defined sequence of amino acids, secondary, ternary and quaternary structure. Despite all of these one may claim that a protein is somewhat disordered since it fluctuates between multiple nearly-degenerate energy minima at the bottom of the folding funnel. These fluctuations are a direct consequence of functional change, more accurately speaking, the need for a possibility of functional change caused by the environmental shifts. These dynamics affects the optical transition frequencies which can be observed by means of different optical techniques. The differences between local protein environments of the pigments embedded into the protein will result in inhomogeneous broadening of the absorption spectra. Spectral hole burning (SHB) technique is a good candidate to overcome the inhomogeneous broadening since it is based on optical line narrowing.

In SHB techniques one employs exciting of the molecule of interest by a narrow-band laser ensuring that only a small fraction of molecules that are in a similar local environment are excited. This fraction has the optical transition frequencies that correspond to the laser wavelength. The process of the excitation followed by the molecule getting stuck in a new conformation is called spectral hole burning process. The manifestation of such a process is a reduction in absorption at the excitation frequency, later on called “burning frequency”, which is referred to as the “spectral hole”.

Spectral Hole Burning techniques may employ two different pathways that are distinguished by the nature of the change caused by the light absorption. The Photochemical Spectral hole Burning leads to the chemical change in the probe molecule. In Non-Photochemical Spectral Hole Burning no chemical change occurs, only a small conformational change of the environment. In our studies we perform the second type (NPHB) to investigate the dynamics and energy barrier distributions of Cytochrome b_6f complex at cryogenic temperatures. This complex plays an important role in photosynthesis and contains naturally embedded Chlorophylls as pigment molecules.

In this study, we focus on studying the protein energy landscapes in the dimeric Cytochrome b_6f with optical spectroscopy, and also investigate the deuteration and detergent effects on the protein. Chapter 2 includes an overview of photosynthesis process and the protein complexes involved in it. A brief description of protein dynamics and protein energy landscapes is provided in Chapter 3. Then, the optical methods used in studying the protein energy landscapes, such as Spectral Hole Burning, and the theory behind these methods are described in Chapter 4. Finally, the experimental results obtained for the Cytochrome b6f protein complex along with the

discussion and the concluding remarks are presented in Chapter 5. The last chapter, Chapter 6, is dedicated to the conclusion of this study and the possible future research.

Chapter 2

Photosynthetic Protein Complexes

Photosynthesis is one of fundamental processes of the ecosystems on Earth. Nearly every oxygen molecule in the atmosphere is released from the water by photosynthesis. For the past 3.5 billion years the Photosynthesis is a main player in oxygenation of our planet and the main mechanism for converting solar energy into chemical energy needed to support life. Thus, for example, according to some studies without oxygenic photosynthesis, the oxygen in the atmosphere would be depleted within several thousand years [86]. In addition, photosynthesis is biologically important in a number of more indirect ways. For instant, in formation of stratospheric ozone or by photosynthetic assimilation of CO_2 and associated processes such as formation of carbonate shells by aquatic organisms [4]. In this chapter I give an overview of the process and its main components and pathways.

2.1 Photosynthesis

Photosynthesis occurs in leaves of higher plants and many kinds of bacteria and algae and to some extent in the stems of the green plants. Plant cells have organelles called chloroplasts that

are actually in charge of the photosynthesis. In the more primitive organisms the apparatus of photosynthesis may be incorporated into the cell membrane. The Photosynthesis has two types: oxygenic photosynthesis and anoxygenic photosynthesis. Oxygenic photosynthesis is the most common and is seen in plants, algae and cyanobacteria. Anoxygenic photosynthetic and oxygenic photosynthetic differ by the electron donors for photosynthesis. Moreover, anoxygenic photosynthesis takes place in only one type of reaction center, in contrast to oxygenic photosynthesis that takes place in two, each of which absorbs a different wavelength of light.[4]

Oxygenic photosynthesis. During oxygenic photosynthesis, light energy is used to transfer electrons from water to carbon dioxide, producing carbohydrates. In this transfer, the carbon dioxide is reduced and the water becomes oxidized. Ultimately, oxygen is produced along with carbohydrates. The photosynthesis process consists of two main classes of reactions. The first requires the presence of light, called “Light reactions”, the second, that does not require the presence of light, - “Dark reactions”.

The very first event in photosynthesis is the light absorption by pigments: chlorophylls (Chl), carotenoids, and phycobilins, contained in antenna protein complexes. The absorbed energy is transferred in the form of electronic excitation energy until it reaches the reaction centers (RCs), located in two large membrane-bound pigment– protein complexes named photosystem I (PSI) and photosystem II (PSII) . Then a pigment molecule in the RC such as Chlorophyll (Chl) releases an electron. The released electron passes through electron transport chain, which ultimately generates the energy (proton gradient) needed to produce ATP (adenosine triphosphate) and NADPH. The “electron hole” in the original chlorophyll pigment in case of PSII is filled by taking an electron from water. As a result, oxygen is released into the atmosphere.

In Light-independent reactions ATP and NADPH are rich energy sources, which drive dark reactions. During this process carbon dioxide and water combine to form carbohydrates like glucose. This is known as carbon fixation. These processes are summarized in Figure 2.1.

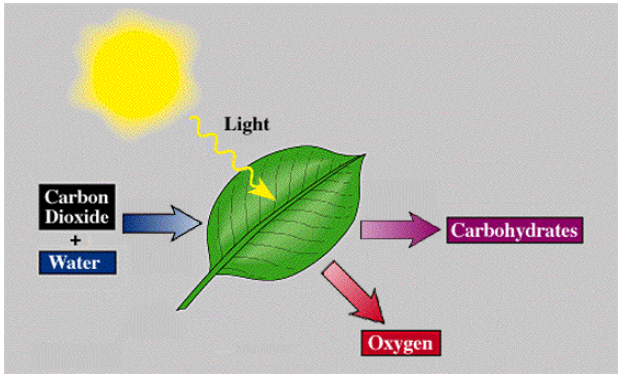

Figure 2.1: The simplified scheme of Oxygenic Photosynthesis: Conversion of Carbon Dioxide and Water into Carbohydrates and Molecular Oxygen using energy of light.[101]

2.2 Electron transfer Pathways

The electron transfer pathway from water to $NADP^+$ is driven by two membrane-bound photosystems. The excitation energy harvested by the antenna is captured by the assembly of unique photoactive Chls molecules, denoted as Reaction Center Chlorophyll in the RC of photosystems (Fig. 2.2).

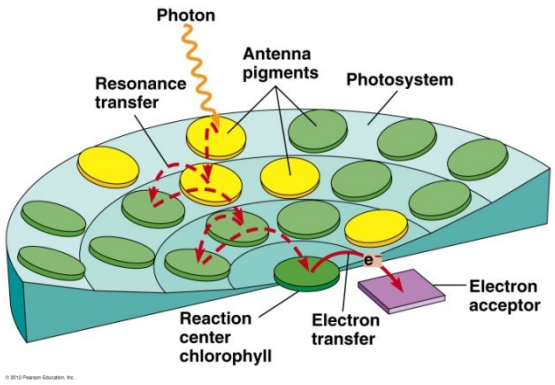

Figure 2.2: Primary steps of energy and electron transfer in photosynthesis.[100].

In PSII, this special photoactive RC is composed of several Chl *a* molecules, dubbed P680, and in PSI, the special RC is a "heterodimeric" complex of Chl *a* and Chl *a'* , dubbed P700. The singlet excited states of these RC Chls (1P∗) initiates the primary photochemistry reaction, that is followed by fast charge separation between excited reaction center chlorophyll and the neighboring primary electron acceptor to form the radical pair.

There are additional protein complexes involved in photosynthetic energy conversion which are also located in the thylakoid membrane. These complexes are the Cytochrome (Cyt) b6f and the ATP-ase (see Fig. 2.3).

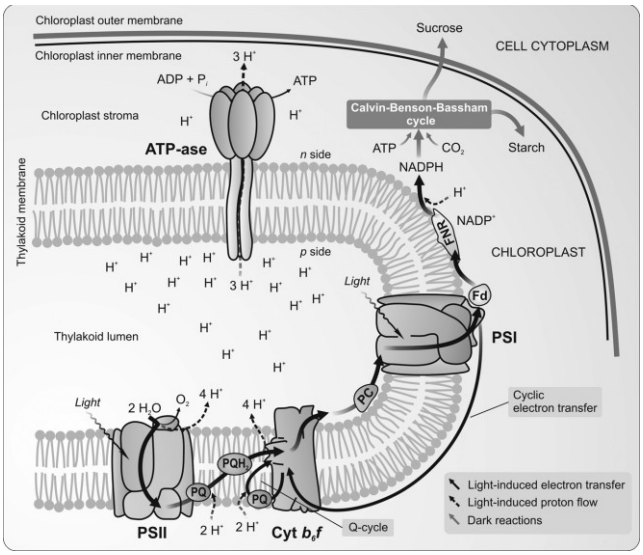

Figure 2.3: A schematic view of the thylakoid membrane and the protein complexes involved in the light-induced electron transfer (black solid arrows) and proton transfer (black dashed arrows) reactions. [4]

Both Photosystems and Cyt b_6f contain almost all the redox-active cofactors that allow light-induced transfer of electrons from H_2O to $NADP^+$ along the thylakoid membrane in the following sequence: $H_2O \rightarrow$ PSII $\rightarrow$ Cyt $b_6f \rightarrow$ PSI $\rightarrow NADP^+$. PSII is linked with the Cyt b_6f complex via the mobile lipophilic hydrogen atom carrier Plastoquinone, in the membrane, while the Cyt b_6f is linked with PSI via a mobile water-soluble redox carrier Plastocyanin in the thylakoid lumen. In addition to these mobile electron transfer carriers, there is a soluble [2Fe-2S]-containing protein ferredoxin (Fd), a one-electron carrier connected with PSI. [4] The scheme that depicts the ETC from water to NADP + via redox-active cofactors is presented by Z-scheme (Fig. 2.4).

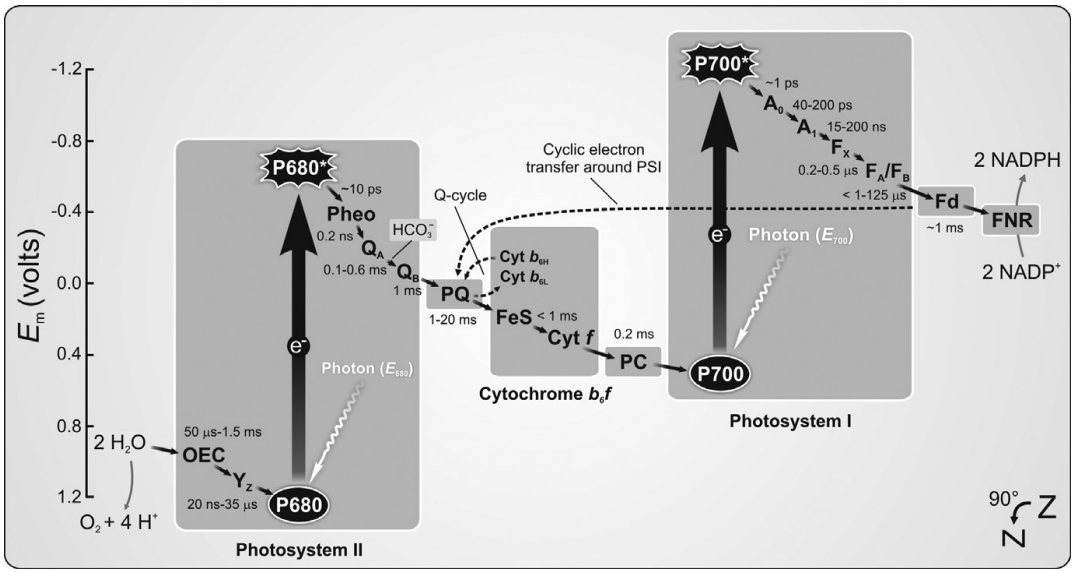

Figure 2.4: The zig-zag or Z-scheme of oxygenic photosynthesis representing the energetics of linear electron transfer from H_2O to $NADP^+$ plotted on the redox midpoint potential (Em, at pH 7) scale. The diagram also shows a cyclic electron transfer around PSI, Q-cycle, and half-times of several linear electron transfer steps. The two black vertical arrows symbolize the excitation of RC Chl a molecules (P680 and P700 in PSII and PSI, respectively); these lead to electrons in the ground state to be raised into a higher (singlet) excited state in response to the absorption of excitation energy from the light-harvesting antenna or by direct absorption of photons (wiggly white arrows. [4]

2.3 Pigments

In green plants there are six main pigments that play an essential role in the photosynthesis process. Pigments are the means by which the energy of sunlight is captured for photosynthesis. However, since each pigment reacts with only a narrow range of the spectrum, there is usually a need to produce several kinds of pigments, each of a different color, to capture more of the Sun's energy. There are three main types of pigments. Each of them has slightly different absorption spectrum that helps to cover and maximize the sunlight absorption (Figure 2.5).

Carotene - an orange pigment
Xanthophyll - a yellow pigment
Phaeophytin *a* - a gray-brown pigment
Phaeophytin *b*- a yellow-brown pigment
Chlorophyll *a* - a blue-green pigment
Chlorophyll *b* - a yellow-green pigment

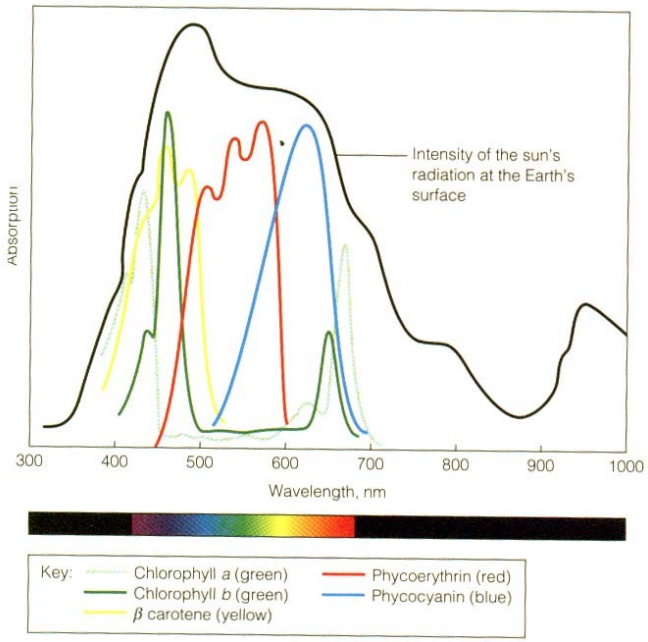

Figure 2.5: The absorption spectra of most common pigments along with intensity of sun radiation.[102]

2.3.1 Chlorophyll

Chlorophyll is the most common pigment that is involved in harvesting light energy. This pigment is found in all oxygenic photosynthetic organisms. The chlorophylls are a group of tetrapyrrolic pigments with common structural elements and functions. In chemical terms they are cyclic tetrapyrroles of porphyrin, chlorine (17,18 –dihydroporphyrin) or bacteriochlorin (7,8,17, 18 – tetrahydroporphyrin). The most common pigments are Chl a and Chl b which differ with respect to both role and relative abundance in higher plants. Chl a/b ratios commonly range from 3.3 to 4.2 in well-nourished sun-adapted species, but can be as low as 2.2 or thereabouts in

shade-adapted species grown at low light. Such variation is easily reconciled with contrasting functional roles for both Chl a and Chl b. [87]

Chlorophyll *a* The Chl *a* is found in any organism that is capable of oxygenic photosynthesis, where it occurs in both reaction centers (RC) and in all light-harvesting complexes (LHC) with very few exceptions[5]. It functions as the primary donor in the RC of PS II, and Chl *a* or a closely related pigment is also the primary donor of photosystem I (PS I)[5]. Chl *a* absorbs strongly in the visible spectrum, but its intense bands are narrow and therefore it must be supplemented by Chls b and Carotenoids in antenna region. Chemical structure of Chl *a* is shown in Figure 2.6.

Chlorophyll *b* Chl b is considered as accessory pigment for Chl a. It slightly differs in chemical structure (See Fig. 2.6) by substitution of methyl group to aldehyde group, resulting in shifted absorbance peaks. In fact it helps better coverage of sunlight emission spectrum, in the same manner as Carotenoids help to absorb from violet to green light. (Fig 2.6)

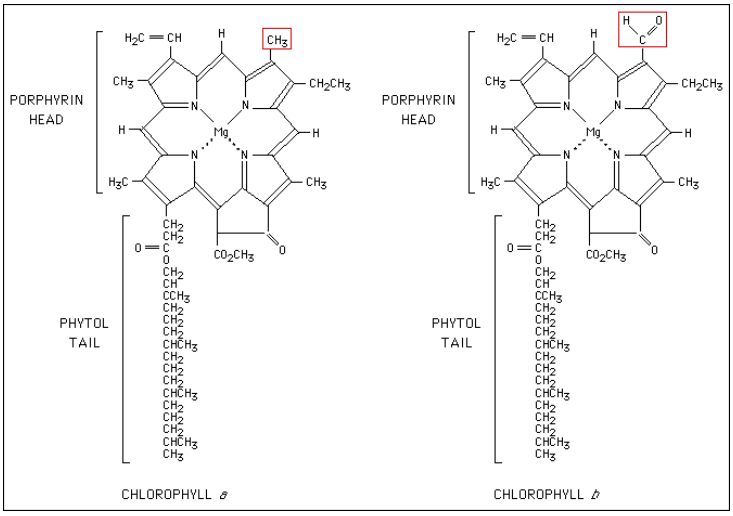

Figure 2.6: Chlorophyll *a* and Chlorophyll *b* chemical structure.[103]

2.4 Protein Complexes of Oxygenic Photosynthesis

2.4.1 Photosystem II (PSII)

In any organism capable of carrying oxygenic photosynthetic PSII functions as a water-plastoquinone oxido-reductase, using light energy to drive the transfer of electrons from water to plastoquinone, resulting in a splitting of water molecule into molecular oxygen and protons. The overall reaction may be shown as: $2\,H_2O + 2\,PQ + 4\,H^+_{\text{stroma}} \xrightarrow{h\nu} O_2 + 2\,PQH_2 + 4\,H^+_{\text{lumen}}$

PSII is a large membrane-integral pigment–protein complex, which exists as a dimer with a total mass of ~700 kDa. [4] Each monomer of PSII contains 20 proteins and about 90 cofactors (mostly pigments). 17 of the proteins are transmembrane subunits and three are peripheral subunits on the lumenal side of the complex. Some of these proteins and major redox cofactors are shown in Figure 2.7. All electron transfer cofactors of PSII are bound to two central transmembrane proteins D1 and D2. These proteins exist as a D1/D2 heterodimer, which, together with a few small proteins, forms the core of the PSII RC. The D1/D2 heterodimer binds two branches of redox cofactors related by pseudo C_2 symmetry. However, the electron transfer within PSII occurs via cofactors located mainly on the D1 side of the D1/D2 heterodimer. Thus this “active branch” contains two Chl a molecules assigned to P680 (PD1 and ChlD1), the primary electron acceptor PheoD1, and the primary PQ electron acceptor QA; the latter is located on the D2 side. [4] Figure 2.7 shows schematic arrangement of central redox cofactors of cyanobacterial PSII monomer.

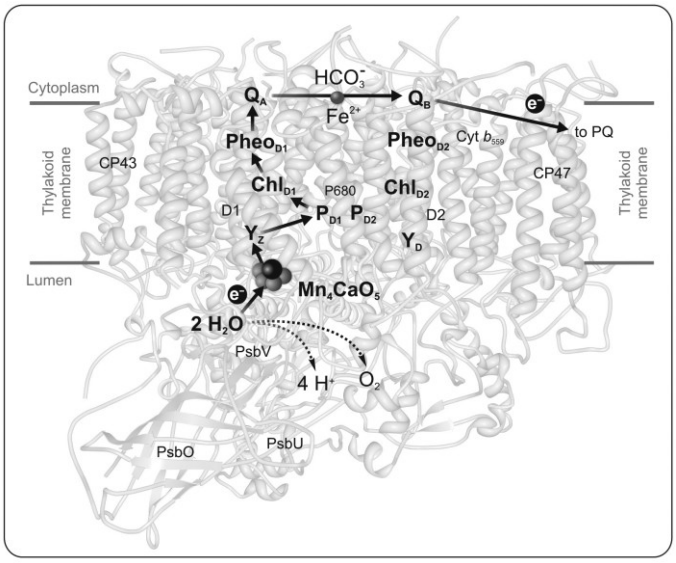

Figure 2.7: A side-on view of cyanobacterial PSII monomer and schematic arrangement of its central redox cofactors. Black solid arrows indicate the direction of electron transfer.[4]

2.4.2 Photosystem I

PSI is a membrane-integral protein complex that is present in all oxygenic photosynthesizers. PSI, just like PSII, is also a main player in converting of light energy for driving the redox reactions of the ETC. Thus PSI uses the energy of light to power the electron transfer from one mobile electron carrier PC (or alternatively Cyt c_6) to another carrier, Fd, and thereby provides the electrons for the reduction of $NADP^+$. It therefore acts as a light-driven plastocyanin: ferredoxin oxidoreductase.[88] In plants, PSI always exists as a monomeric complex, however in cyanobacteria PSI exists mainly as a trimer having a molecular weight of ~1100 kDa.. PSI monomer contains 12 proteins and about 130 noncovalently bound cofactors. [89, 90] The core of the PSI complex is formed by two proteins, PsaA and PsaB. These two proteins coordinate the

majority of the cofactors of the ETC within PSI, as well as most of the antenna Chls and the Cars of PSI. Moreover, PsaA/PsaB heterodimer is known to be involved in the docking of the mobile electron carrier (PC or Cyt c_6) near P700 on the electron donor (lumenal) side of PSI. Figure 2.8 shows schematic arrangement of the central redox cofactors of PSI.[4]

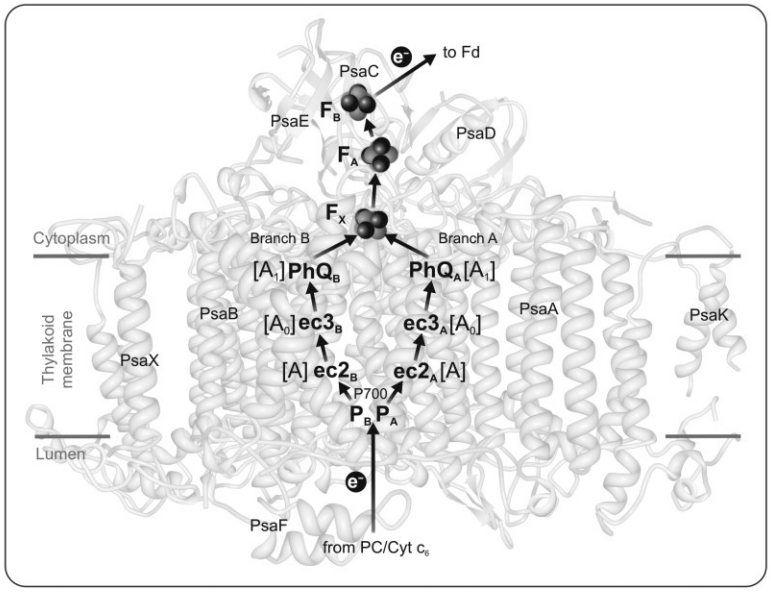

Figure 2.8: A side-on view of cyanobacterial PSI monomer and schematic arrangement of its central redox cofactors. Black solid arrows indicate the direction of electron transfer. Only a few proteins of PSI are shown. For further discussion and abbreviations, see text. Adapted from Shevela et al. [85]

2.4.3 Cytochrome b_6f

Light-induced electron transfer between the two photosystems is mediated by the membrane-integrated Cyt b_6f complex; here, this complex catalyzes the transfer of electrons from lipophilic PQH_2 to the soluble PC. Moreover, the intersystem electron transport performed by the Cyt b_6f complex is coupled with the transport of protons from the stroma to the lumen, thus contributing to the generation of a proton gradient, and an electrochemical potential across the thylakoid

membrane that is further utilized by the ATP synthase for ATP synthesis. In both cyanobacteria and plants, the Cyt b_6f complex exists as a dimer and contains several prosthetic groups. Each monomer is composed of eight subunits.[84] These consist of four large subunits: a 32 kDa cytochrome f with a c-type cytochrome, a 25 kDa cytochrome b6 with a low- and high-potential heme group, a 19 kDa Rieske iron-sulfur protein containing a [2Fe-2S] cluster, and a 17 kDa subunit IV; along with four small subunits (3-4 kDa): PetG, PetL, PetM, and PetN. The total molecular weight of the dimer is 217 kDa. When PQH_2 is oxidized by the FeS protein, protons are released into the lumen. One of two available electrons delivered by PQH_2 passes along a linear ETC to the Cyt f subunit and further to a small mobile PC (or Cyt c_6), which then carries the electron toward PSI. The other electron is transferred through the two Cyt b_6 hemes, which then reduces a PQ to PQ^- (semiquinone). Upon receiving one of the two electrons from a new PQH_2 molecule (oxidized by the FeS), PQ^- is reduced to PQ^{2-} at the same time picking up two protons (and forming PQH_2), participating thereby in a cyclic process called the Q-cycle. Thus the Q-cycle increases the number of protons pumped across the membrane (Fig. 2.3). Overall, for every two electrons that reach PSI, four protons are translocated across the thylakoid membrane. Figure 2.9 depicts the Cyt b_6f structure. [4]

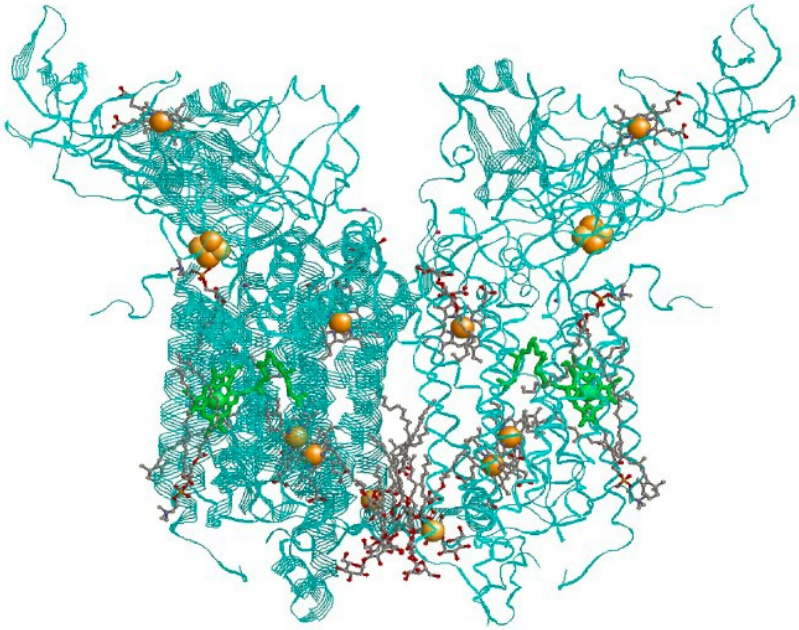

Figure 2.9: Structure of the Cytochrome b_6f dimer. PDB ID: 2E74 Chlorophyll *a* molecules are highlighted in green. Iron atoms of hemes and iron-sulfur clusters are highlighted in gold. [93]

2.5 Excitation Energy Transfer

As it was mentioned before, the primary process in photosynthesis starts with the absorption of the light by the pigments. These pigments have strong overlap of their fluorescence bands with absorption band of the same or others type pigments (Figure 2.10), creating favorable conditions for excitation energy transfer between them in accordance with the Förster theory.[91]

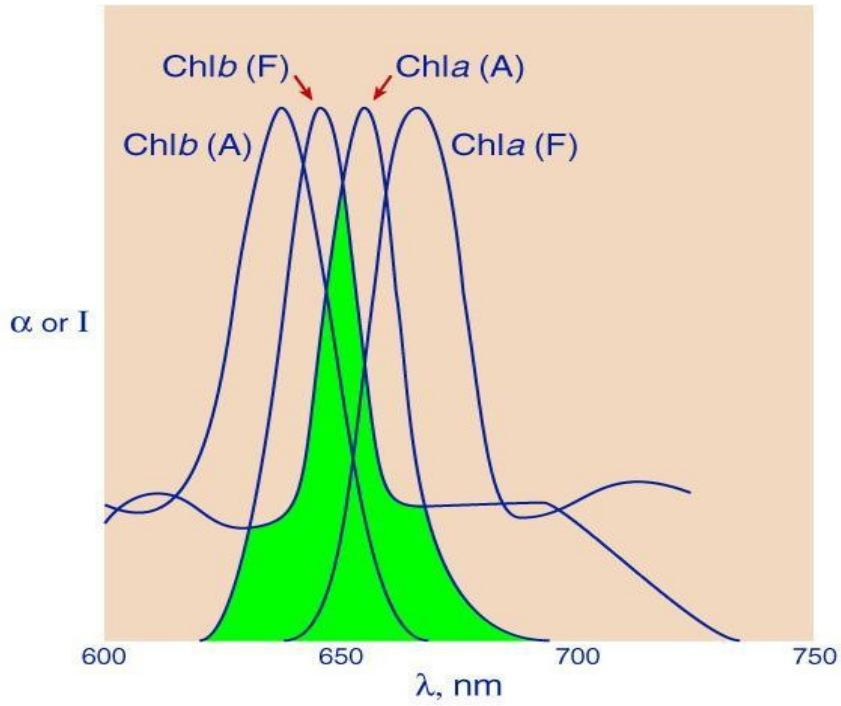

Figure 2.10: Overlapping of absorption band *(A)* of Chl *a* and fluorescence band *(F)* of Chl *b* (shaded area), and of the absorption band of Chl b and emission and of Chl a.[94]

Förster resonance energy transfer (FRET) theory states that excitation energy transfer probability is inversely proportional to R^{-6} due to the induced dipole – induced dipole coupling mechanism.

That probability E (transfer efficiency) is given by Equation 2.1:

$$E = \frac{R_0^6}{R_0^6 + R^6} \quad (2.1)$$

where R is the distance between the donor and the acceptor pigments and R_0 is the Förster radius. Förster radius is determined as a distance at which the energy transfer efficiency reaches 50%. FRET efficiency depends through R_0 on many physical parameters such as:

- The distance between the donor and the acceptor (typically in the range of 1–10 nm)

- The spectral overlap of the donor emission spectrum and the acceptor absorption spectrum (Figure 2.10)
- The relative orientation of the donor emission dipole moment and the acceptor absorption dipole moment.[92]
- The dielectric constant of the environment surrounding the interacting pigments. It is particularly important to distinguish between pigments in water (high dielectric constant) and protein (low dielectric constant) environments.

Chapter 3

Protein Dynamics

The proteins are complex organic molecules, which carry out many different functions in living organisms. In vivo the protein are folded into tertiary and, in some cases into quaternary structure providing the desirable functionality. The folding of proteins is a complicated process that must be guided by some rules in order to avoid the Levinthal's paradox. Trying to fold the protein into correct configuration by random folding could probe an astronomical number of possible conformation, therefore to attain the right conformation by sequential probing would require approximately the life time of the universe. Couple of theories were proposed to explain the surprisingly high speed of protein folding, compared with a random sampling mechanism, e.g. the framework model, the nucleation-growth mechanism, the diffusion-collision mechanism, the hydrophobic collapse model and the energy landscape (folding funnel) model.[2] By the end of the process the protein always reaches its native state, or, more precisely, a collection of energetically close native states. The fluctuation between these state are governed by the Protein Energy Landscape, a concept proposed by by Joseph Bryngelson and Peter Wolynes.[99] The conformational changes have a direct impact on the function of a protein. These functions of proteins depend on vast majority of the factors such a surrounding solvent, pH, coenzyms etc. All of these could lead to protein structure fluctuation in its tertiary structure, and ultimately to conformation change.

3.1 Protein Energy Landscape

Switching from one conformational state to another requires some amount of energy to overcome the barrier. The distribution of the local minima and the potential barriers along some generalized coordinates determines the energy landscape. However, deriving the absolute, exact landscape is nearly impossible task since protein is a complex molecule containing a long chain of aminoacids and folded into secondary, tertiary and quaternary structure. Moreover, in contrast to crystal lattice, the protein is a somewhat amorphous substance which complicates it even more. Nevertheless, in accordance with the folding theory [13,14], the stable - native state of a protein is relatively well defined with limited number of substates. Figure 3.1. These substates represent local energy minima which are separated by potential barriers that need to be overcome for the conformational substate switch. Taking the degree of freedom of a protein as generalized coordinate with associated minima and potential barriers one may form the Protein Energy Landscape PEL).

In other words the PEL is a statistical description of a protein's potential surface. It assumes that folding occurs through organizing an ensemble of structures rather than through only a few uniquely defined structural intermediates. It suggests that the most realistic model of a protein is a minimally frustrated heteropolymer with a rugged funnel-like landscape biased toward the native structure. This statistical description has been developed using tools from the statistical mechanics of disordered systems, polymers, and phase transitions of finite systems.[13]

3.2. Protein Folding

Nowadays protein folding process is best described by folding funnel hypothesis, which is a specific version of the energy landscape theory of protein folding. This theory assumes that the

native state of a protein corresponds to its free energy minimum under the surrounding conditions. It also suggests that the energy landscape may be rough with many local minima that correspond to partly folded protein in which it can be trapped during a folding.[14,15] Figure 3.1 shows landscape parameters for a realistic protein folding funnel.

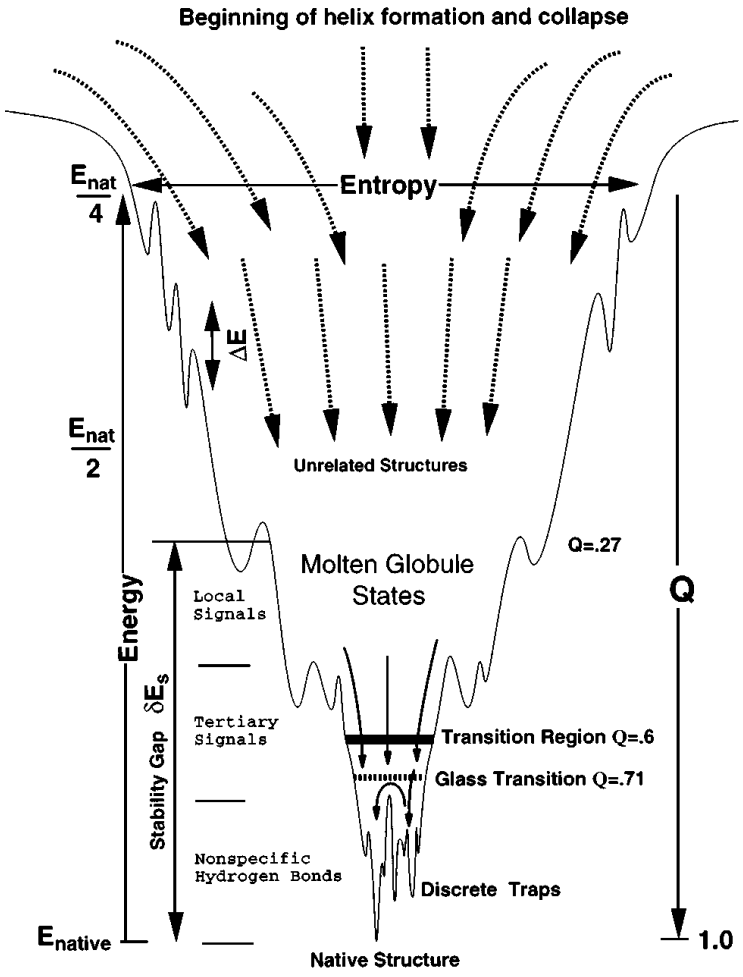

Figure 3.1 A viable protein folding landscape. The rugged folding landscape of a small helical protein is funnel-like, with a preferred direction of flow toward a unique native state. The order parameters *E*, the solvent-averaged energy, and *Q*, the fraction of native-like contacts, describe the position of an ensemble of states within the funnel and stratify the landscape. The fluctuations 1*E* and the stability gap _*E*s between the compact misfolded or molten globule states and the native state are functions of these order parameters and can be estimated using theory and experiment. [16]

3. 3. Protein energy landscape near the energy minimum

In this work we focus only on the native structure of the protein which is represented not by only one possible state, but, as it was mentioned before, but a set of several nearly-identical ones One can zoom in to the native structure in Figure 3.1 to explore the energy minima around the native state. Potential energy in amorphous materials like protein or glass has several different local minima. (Figure 3.2) Each minimum represent a specific molecular configuration, however this figure shows just two generalized coordinate while in realty the energy landscape may be multidimensional.

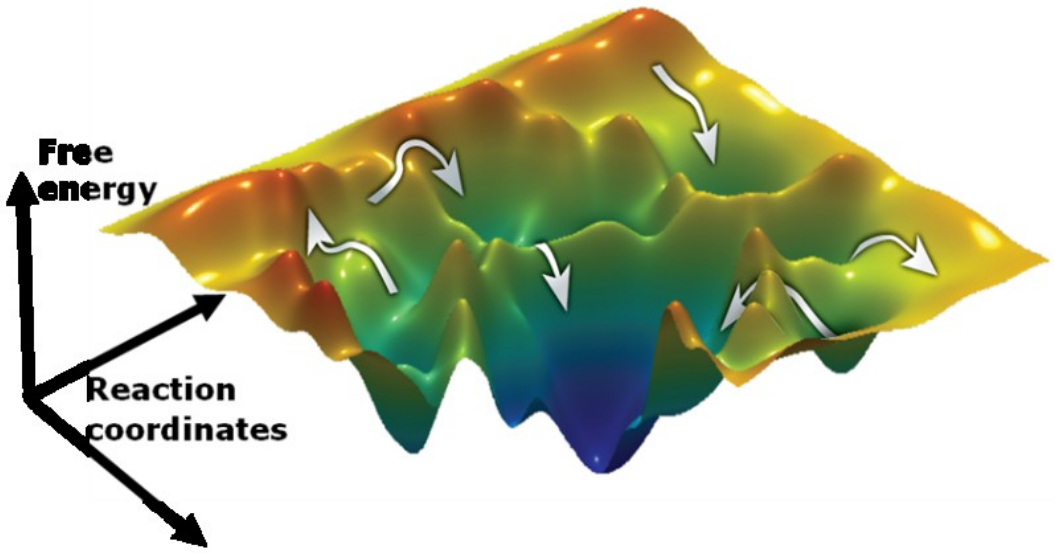

Figure 3.2: Protein energy landscape with two generalized coordinates

3.4. Two Level System

Even a relatively sample protein is a complex molecule with multiple degrees of freedom such as backbone angles, ligand angles, lengths of the bonds etc, thus it looks unrealistic to form a complete PEL. Lowering temperatures will gradually freeze out most of these degrees of freedom, yet the protein will still somehow move due to thermal fluctuation, exciton-phonon interactions and many other factors even at cryogenic temperatures.

Two Level System (TLS) is a simplified model that may be applied to the conformational changes in the proteins and that represents the energy landscape with only one generalized coordinate. This model is especially useful in case when the protein is well known to have two significant well-defined conformations. A good example of such protein may be Myoglobin. [96,97]

Initially this model was devised to explain unusual behavior of various thermodynamic parameters of amorphous solids at low temperatures [53], such as heat capacity, heat conductivity, etc, however it does not provide direct information about the entities involved in conformational change. Figure 3.3 shows the schematic representation of TLS.

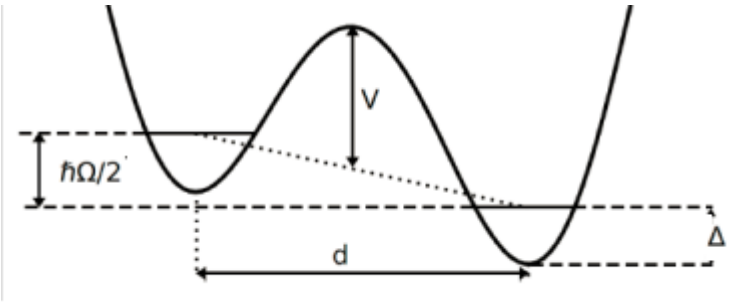

Figure 3.3: Two Level System model

There are two local energy minima, separated by the distance *d,* potential barrier with the height *V* and asymmetry Δ. The asymmetry parameter represents the difference between two zero levels of the phonon/vibrational mode of each local minima. The parameter $\hbar\Omega/2$ represents the minimal quantum-mechanical vibrational energy in each well.

The properties of amorphous or glassy material are determined by the fact that they have short range atomic order without the long-range order. Despite the randomness of the atomic arrangements, and even independent of their chemical composition, most amorphous solids display surprising similarities in their properties at temperatures below a few Kelvin. This universality is typically explained via the so-called standard tunneling model (STM)[98]. The standard tunneling model makes the following key assumptions • The TLS can exist in one of two energetically similar configurations. • These configurations are modelled as two minima in a double-well potential which are separated by a barrier. • At sufficiently low temperatures, thermal activation over the barrier is suppressed and the dynamics are governed by quantum tunneling through the barrier. • In general, the system couples to applied electric or strain fields in such a way that transitions can be driven between the states. • Due to the random atomic arrangements, an ensemble of TLS is characterized by a wide distribution of potential barrier heights and thus spans a large range of switching rates and eigenenergies.

Thus, double –well potential (TLS model) is very practical tool to be applied to amorphous solids and glasses to describe their dynamic properties. For many different proteins having two main conformational substrates this approach may yield good result in probing the PEL. [18] The question remains if such oversimplified model could be useful for describing the properties of proteins that do not have two well-defined states with distinct functions.

The system must surmount the potential barrier to switch from one configurational state to another. At all but the lowest temperatures, the transition between two states may be done either by the process of barrier hoping or by tunneling process through the potential barrier, Figure 3.4. Both processes require certain amount of energy in the system being available for the purpose of the conformational change, but the amounts of energy and underlying mechanisms are vastly different.

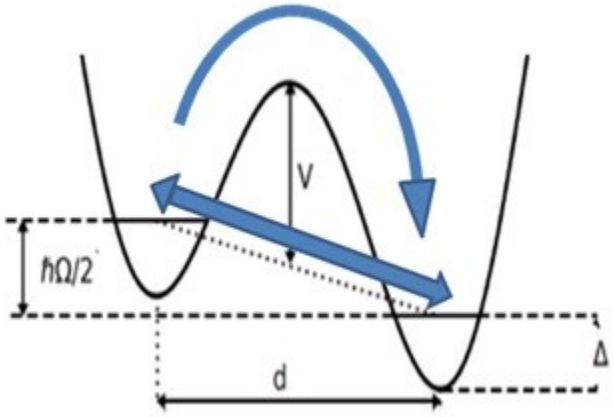

Figure 3.4: Barrier hopping and tunneling in the TLS

At low temperatures (below 10K-12K) the tunneling is observed to be the dominant process in transition between these two states. The tunneling parameters λ then can be expressed in terms of the potential barrier height V and other barrier parameters: Equation 3.1

$$\lambda = \frac{d}{\hbar}\sqrt{2mV} \quad (3.1)$$

Here m is the effective mass of the tunneling entity and d is a distance between two local minima.

Chapter 4

Theory of Spectral Hole Burning

In this chapter all theory regarding spectral hole burning which is used in this thesis is discussed, including different types of this method and the process of determining the protein energy landscape parameters in both the ground and excited states of pigment-protein systems. Originally SHB evolved from the optical spectroscopy of intramolecular electronic and vibronic energy levels of organic molecules in the solid, which is actually the framework to handle them. The first observations of persistent hole burning were done in 1974 by Kharlamov et al. in organic glasses and by Gorokhovskii et al. in organic crystals. While the method became more sophisticated and the spectral resolution was increased, the necessity arose to understand the details of the interactions of the dye molecules with their surrounding matrix in order to describe the measured spectra. After that it was only the next logical step to turn the purpose of the experiment upside down and employ the molecules as probes for the properties of their surrounding matrix - spectral hole burning became a tool of solid state physics. This step was of course not as straightforward as described here. Efforts had to be made to understand the basics of what was observed. But finally spectral diffusion was discovered and confirmed in a number of investigations. Since then the technique of spectral hole burning has developed into a highly efficient method especially suited for the investigation of the low temperature tunneling dynamics in organic amorphous solids.[22]

4.1 Spectroscopy of the Impurity Centers in Solids

Spectral hole burning is the frequency-selective bleaching of the absorption spectrum of a material, which leads to an increased transmission (a "spectral hole") at the excitation frequency. This technique generally relies on the presence of “impurity centers” in the solids and their manifestations by the means of optical spectroscopy. In that process normally smooth inhomogeneously broadened absorption bands in solids at low temperatures can be spectrally modified for time periods much longer than the lifetime of any excited state. There are a number of fundamental requirements needed to perform SHB.[7]

- The optical absorption spectrum of the guest (impurity) molecule under consideration must be inhomogeneously broadened,
- There must exist more than one ground state configuration of the total system (host + guest/impurity/probe),
- The optical absorption frequencies for transitions from the various ground states must differ by more than the linewidth of the tunable light source in use.
- There must exist an optical pumping pathway that connects the ground state configurations.
- The relaxation among the ground state configurations must be much slower than the decay rate of any excited state.

In order to be able to decipher a multimolecular guest spectrum in a host solid one should first consider the spectrum of single molecule in vacuum, which is a narrow line whose width is determined by the excited state lifetime. This absorption line has Lorentzian line shape with Full Width at Half Maximum (FWHM) as follows:

$$\gamma_{nat}(cm^{-1}) = \frac{1}{2c\pi\tau_1} (4.1)$$

where τ_1 is an excited state life time in *ps* and *c* is speed of light.

However if the guest molecule is located in a solid, the spectroscopic measurement will be affected by the presence of phonons which originate from the lattice vibration of the solid. Vibronic transition where the energy of an absorbed photon is divided between electronic and vibrational transitions, will affect the shape of absorption spectrum of an isolated molecule in accordance with Franck-Condon principle. However, at low enough temperature this spectrum will still feature a narrow Zero-Phonon Line. (black feature labeled with 0-0 in Figure 4.1)

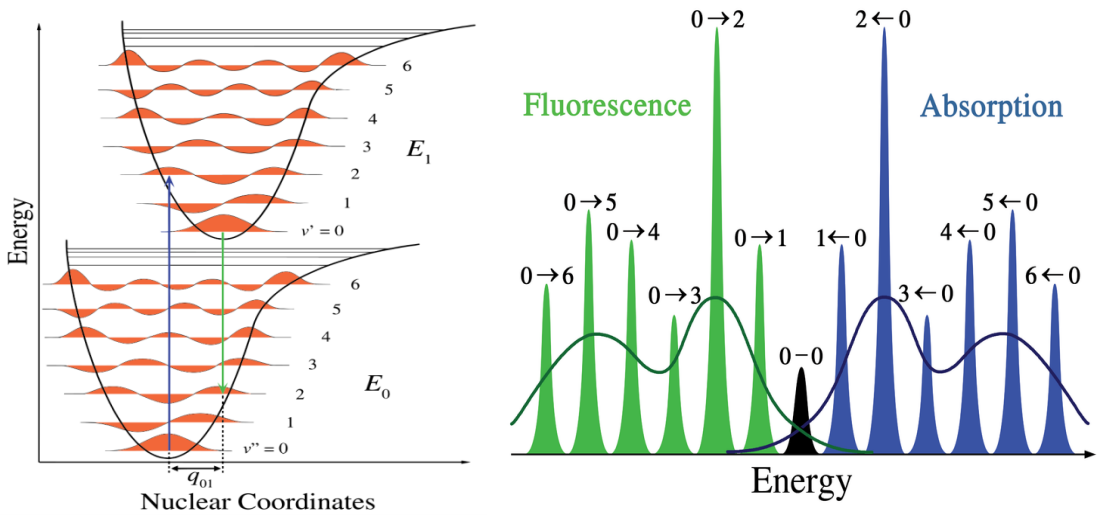

Figure 4.1. Franck–Condon principle energy diagram. Since electronic transitions are very fast compared with nuclear motions, vibrational levels are favored when they correspond to a minimal change in the nuclear coordinates. Depicted energy diagram shows situation favoring transitions between v = 0 and v = 2.[103]

Vibtational relaxation may take place between the vibrational levels in both excited and ground state. The relative intensity of ZPL is defined by Debye-Waller factor α:

$$\alpha = \frac{I_{ZPL}}{I_{ZPL} + I_{PSB}} \quad (4.2)$$

where I_{PSB} is the integral intensity of the Phonon Sideband (PSB) and I_{ZPL} is the integral intensity of the ZPL. On the other hand Debye-Waller factor depends on the linear electron-phonon coupling (Huang-Rhys factor) S as:

$$\alpha = \exp(-S \times \coth(\frac{\Omega_M}{2k_B T})) \quad (4.3)$$

where Ω_M is the PSB peak frequency that represents the difference between maximum energies of ZPL and PSB, T is absolute temperature and k_b is the Boltzmann constant. As it was mentioned above at cryogenic temperatures the absorption spectrum is dominated by ZPL, and the overall tendency of the temperature dependency is shown in Figure 4.2

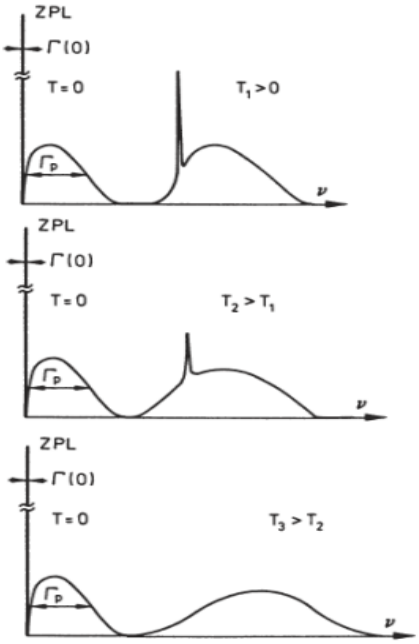

Figure 4.2: Dependence of ZPL and PSB on temperature. From [7]

The width of the ZPL corresponds to the minimum absorption linewidth of the guest molecule in the host environment. This width called Homogenous Linewidth Γ_{hom}.(Figure 4.3)

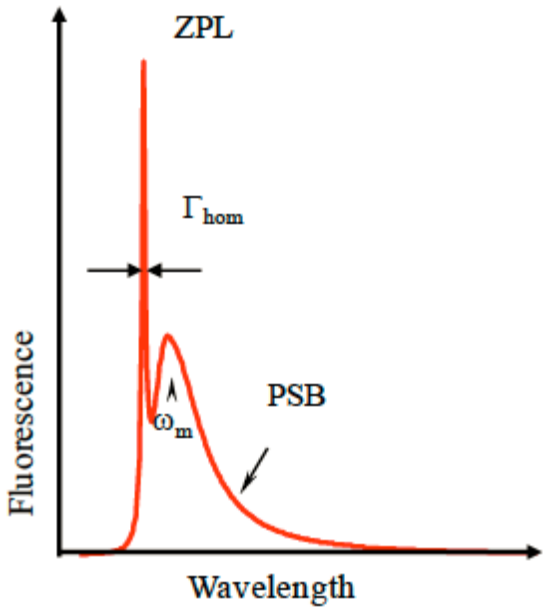

Figure 4.3: Absorption spectrum of a single molecule in solid, including ZPL and PSB.[8]

Homogenous Linewidth is given by equation 4.4 :

$$\Gamma_{hom} = \frac{1}{\pi\tau_2} = \frac{1}{2\pi\tau_1} + \frac{1}{\pi\tau_2^*(T)} \quad (4.4)$$

where τ_2 is total dephasing time. It is also sometimes called the excited coherence life time consisting of excited state lifetime τ_1 and the pure dephasing time $\tau_2^*(T)$. The excited state lifetime τ_1 is the time that the system spends in the excited state before relaxation occurs and pure dephasing time (τ_2^*) reflects the decay of the phase coherence of the superposition state initially created by the photon [3]. It should be noted that the pure dephasing time here is given

as a function of the temperature, since is strongly depends on it. The pure dephasing time (τ_2^*). at absolute zero is infinitely long, but even at liquid helium temperatures it cannot be neglected. Now the absorption of light by identical molecules embedded in an optically transparent perfect crystal can be considered (Fig 4.4). The relevant quantum-mechanical system consists of the electronic and vibrational degrees of freedom of the molecule (impurity center) and of the vibrational motion of the surrounding solid. Since the environment of all the molecules is the same and in assumption that they are far away from each other to ensure there are no interaction between them, they will absorb light on the same frequency.

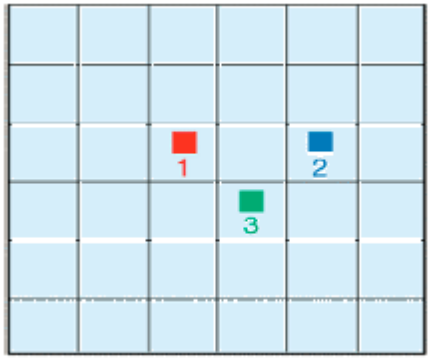

Figure 4.4: The lattice structure of a perfect crystal with doped guest molecules.[8]

Moving forward to more realistic scenario one may place the guest molecules into real – not perfect – solid (Figure 4.5). As a result each of the guest molecule will be exposed to a slightly different surrounding which will be manifested by inhomogeneous broadening of the ensemble spectra (Figure 4.6). The protein at cryogenic temperatures must be considered as such an imperfect crystal and to overcome this issue Spectral hole burning technique may be employed.

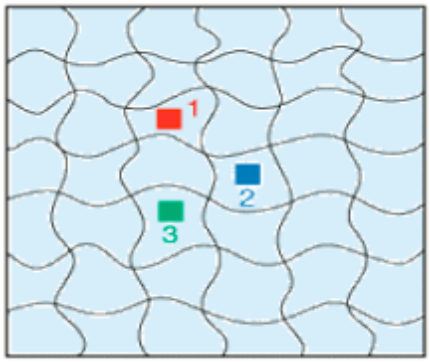

Figure 4.5: The lattice structure of an amorphous solid doped with guest molecules [8]

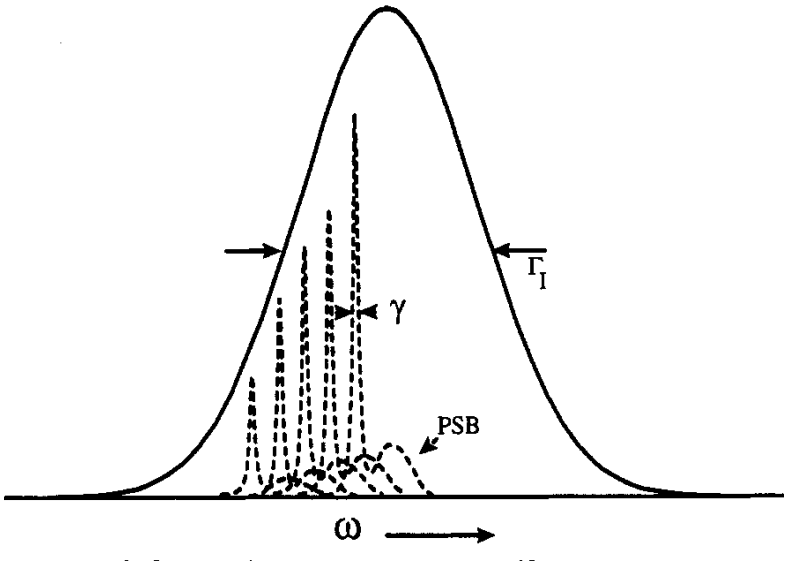

Figure 4.6: Schematic representation of homogeneous (7) and inhomogeneous (Ti) broadening. Profiles of the zero-phonon lines (ZPL) and their associated sidebands (PSB) for specific sites at different frequencies have been enlarged compared to the inhomogeneous line to provide more detail.[10]

To produce the real absorption spectrum of the amorphous host one should convolve the Site Distribution Function (SDF) which is the distribution of probabilities of ZPL transition of guest molecules with the Single Site Absorption (SSA) which is an absorption of the single guest molecule including ZPL and PSB.[36] The process is shown in Fig 4.7

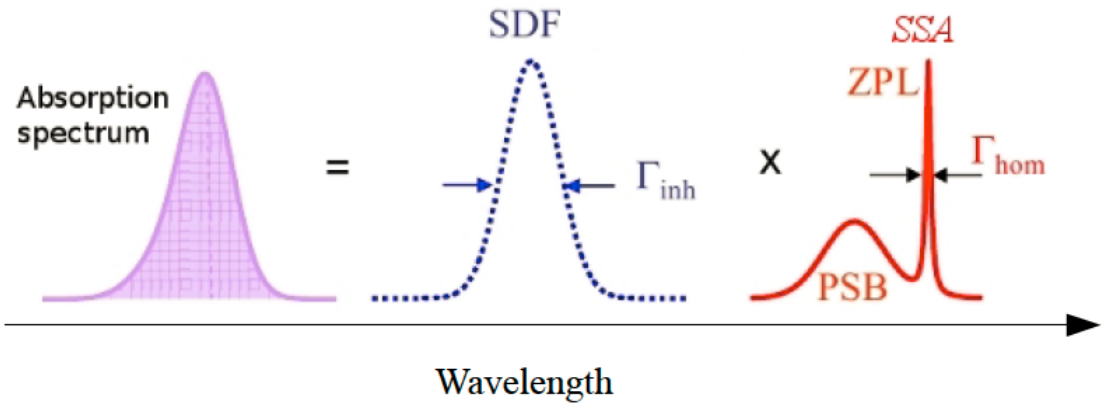

Figure 4.7: The slightly asymmetrical absorption spectrum as a result of convolution of a Single Site Absorption and Site Distribution Function. [8] [9]

4.2 Spectral Hole Burning

As was previously discussed a protein in general is a complex molecule or complex of molecules that has very well defined sequence of amino acids, secondary, ternary and quaternary structure. Despite that one may claim that a protein is disordered since it possesses multiple energy minima between which it can fluctuate. These dynamics affect the optical transition frequencies which can be observed by means of various optical techniques. Taking into consideration the fact that each pigment is sensitive to its environment one should overcome the effect of inhomogeneous broadening in the absorption spectra. Spectral hole burning (SHB) technique is suitable for this purpose.

In SHB techniques we excite the molecules of interest by a narrow band laser ensuring this way that only a small fraction of pigment-protein systems that are in similar states are excited. This fraction has the optical transition frequencies that correspond to the laser band. Excitation may

trigger a small conformational change in the protein leading to system being stuck in the new conformation. Thus it results in reduction in absorption at burning frequency, which in turn produces a spectral hole. (Figure 4.8)

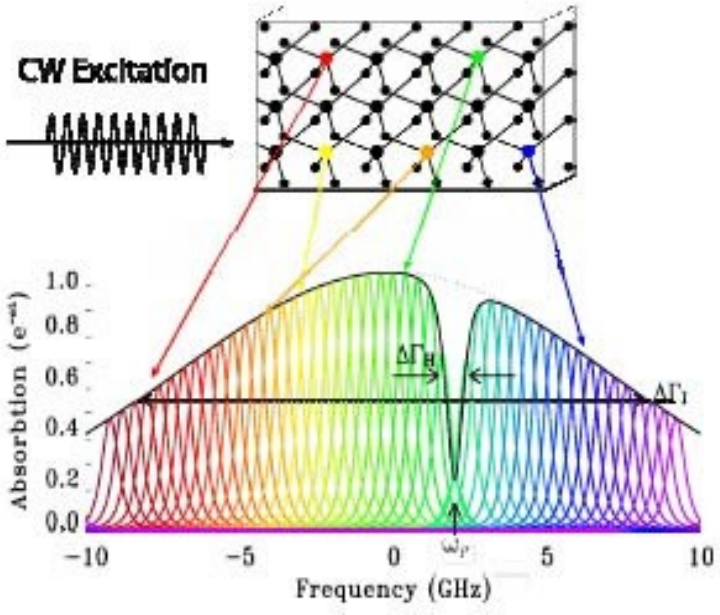

Figure 4.8.1: Normalized spectral absorption profile of a SHB crystal with a spectral hole burned at ω_P. $\Delta\Gamma_I$: inhomogeneous bandwidth. $\Delta\Gamma_H$: homogeneous linewidth.[11]

Spectral Hole Burning techniques may employ two different pathways that are distinguishing by the nature of the change caused by the light absorption.

The Photochemical Spectral Hole Burning is a process in which the absorption leads to a chemical change in the molecule of interest causing most likely irreversible change. On the contrary, in Non-Photochemical Spectral Hole Burning (NPHB) no chemical change occurs, but physical and structural changes in the host environment are considered to be a reason for a hole

production. In other words, conformational change induced by the light of burning frequency will be reflected by the means of spectroscopic measurements.

The Hole Burning Spectrum may be found using Equation 4.5:

$$HBS = A(\Omega,t) - A(\Omega,0) \quad (4.5)$$

where A(Ω,*0*) is the pre-burn spectrum and A(Ω,*t*) is the spectrum after burning for time *t*.

The simplified sketch of post-burn and pre-burn spectra is shown in Figure 4.8. It is easy to see that the main hole feature is an image of ZPL in the absorption spectrum. The Antihole represents the products of Non-Photochemical Burning, while Real PSHB stands for Phonon Side Band of burnt resonant molecules (molecules that were burnt through ZPL) , and Pseudo PSHB is made of the ZPL of the molecules that were burnt through their PSB. As a result, all of those molecules vanished from the absorption spectrum producing a hole with two wings.

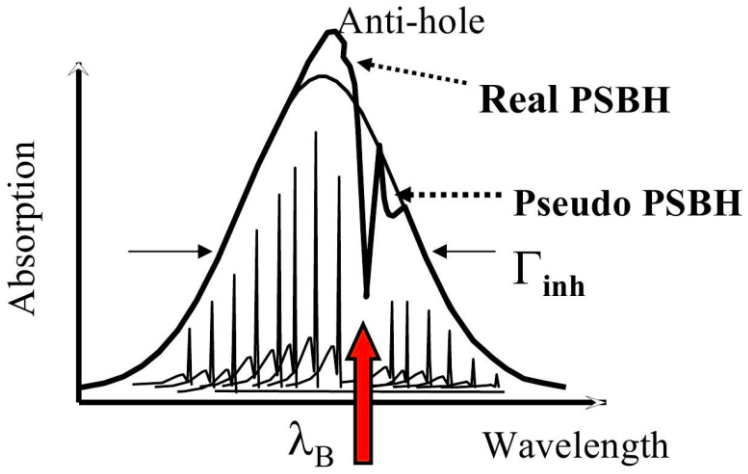

Figure 4.8.2 The different features of NPHB including ZPH, real PSBH, and pseudo PSBH [35]. Using the term photoproduct is not the best choice for NPHB. [8]

SHB is an ensemble technique and any single molecule in the fraction that is in resonance with the burning frequency has some probability to be excited and to be burned out, therefore we can observe gradual growth of the spectral hole. In order to describe this process Fractional Hole Depth (FHD) is introduced. Equation 4.6:

$$FHD = 1 - \frac{A(\Omega,t)}{A(\Omega,0)} \quad (4.6)$$

For small fractional hole depths the dependence of the burnt hole width to the homogenous hole width is represented by Equation 4.7 :

$$\Gamma_H = 2\Gamma_{\text{hom}} = \frac{2}{\pi\tau_2} = 2\left(\frac{1}{2\pi\tau_1} + \frac{1}{\pi\tau_2^*(T)}\right) \quad (4.7)$$

The factor of 2 results from the fact that a convolution of two Lorentzians has the width that is the sum of the widths of the original Lorentzians. In the case of SHB, the modified SDF with the hole with the width Γ_H is convoluted with the single-molecule spectrum whose ZPL has the same width, yielding $\Gamma_H=2\Gamma_{hom}$

Finding the fluorescence life time (τ_1) looks very straightforward in theory, yet practically even at very low temperatures the pure diphasing time (τ_2^*) has dominant effect on the line or hole width, even though at absolute zero it is infinitely long [95]. Consequently other technique must be applied to determine (τ_1).

Figure 4.7 shows the concept of modeling real absorption spectrum which is, as it was mentioned before, result of the convolution of SDF with SSA, while the SDF is modified following the burning. Under assumption that the linewidth of the laser is much narrower than the homogeneous width, the post burn spectrum is given by the master Equation 4.8

$$A(\Omega,t) = 1.5\int d\omega L(\Omega-\omega)G(\omega)\int d\lambda f(\lambda)\int d\alpha \sin(\alpha)\cos^2(\alpha)e^{-Pt\sigma\phi(\lambda)L(\omega_B-\omega)\cos^2(\alpha)} \quad (4.8)$$

This is the post-burn absorption spectrum after burning at ω_B, with photon flux P for time t, $G(\omega)$ is pre-burn SDF (usually Gaussian), $L(\Omega-\omega)$ is the SSA consisting of ZPL and the PSB with total area normalized to one on the frequency ω scale. λ is the tunneling parameter while $f(\lambda)$ is the distribution of λ in the excited state of the pigment-protein system (see next section). This distribution is usually considered as Gaussian with mean value of λ_0 and standard deviation of σ_λ.[84] α is the angle between the polarization of the laser and the transition dipole vector of the chromophore , σ in the exponential is the integrated absorption cross-section of the chromophore.[35] $\phi(\lambda)$ is a quantum yield of non-photochemical hole burning which is given by Equation 4.9

$$\phi(\lambda) = \frac{\Omega_0 \exp(-2\lambda)}{\Omega_0 \exp(-2\lambda) + \tau_1^{-1}} \quad (4.9)$$

where Ω_0 is the attempt frequency, which defines how often system tries to pass the potential energy barrier between two wells in TLS model by tunneling. The attempt frequency is considered to be on the order of 10^{12} Hz. [20]

4.3 The Mechanism of NPHB

NPHB mechanism for amorphous solids is based mainly on the Two-Level System (TLS) model that is employed to explain anomalous specific heat and heat conductivity in glasses at low temperatures. However, in our case there are two TLS – for the excited electronic state and

ground state of the guest molecule. On should note that this model is simplified and actual number of the minima of the protein energy landscape is greater than two shown in Figure 4.9

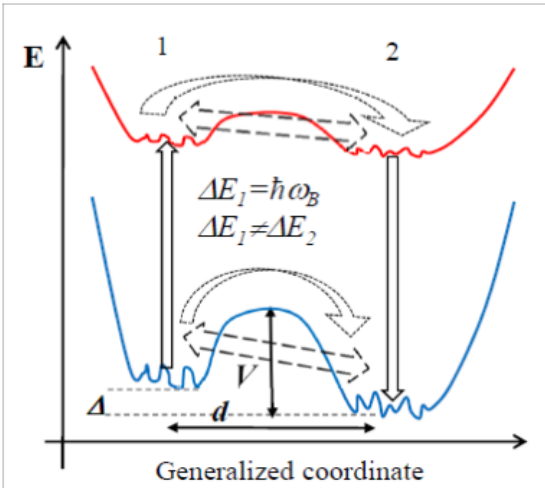

Figure 4.9: Schematic representation of TLS for NPHB

After the absorption of a photon the system that initially was in the minimum 1 of the ground state may be excited to the minimum 1 of the excited state, and then if the barrier height in the excited state of the system is significantly lower then in the ground state there is a non-negligible probability of transition from the minimum 1 to the minimum 2 in the excited state. The following relaxation will take the system into minimum 2 in the ground state and it will stay there for some significant time period which will be defined by the ground state barrier parameters. In figure 4.9 parameter $\Delta E_1=\hbar\omega$ corresponds to the burning frequency and the energy difference between corresponding wells of excited/ ground state is shown. The overall process will result in a light-induced transition from the minimum 1 of the ground state to minimum 2 of the ground state. It should be noted that the transition in the excited state may occur only during of the fluorescence life time. As a result of the transition one can observe the shift in the absorption spectrum of the chromophore. As it was explained before the transition

between two substates may be either by hopping or by tunneling, yet at low enough temperatures NPHB occurs mainly due to tunneling. Tunneling process is phonon assisted process since there is an energy gap between two wells; however the chromophore-protein system may not just lose some energy but also acquire some, depending on the energy of the new state. Thus we can introduce such concepts as downhill transition and uphill transition. As a result of the uphill transition the scattered lattice phonon would lose some energy, while during the downhill transition the phonon gains some. The rate of uphill tunneling is always lower then the rate of downhill tunneling. The downhill rate is given by Equation (4.10)

$$R_{downhill} = \frac{3f^2W^2E}{16\pi\rho c^5\hbar^5}(n(E',T)+1) \quad (4.10)$$

while for uphill process it is given by Equation 4.11:

$$R_{uphill} = \frac{3f^2W^2E}{16\pi\rho c^5\hbar^5}n(E',T) \quad (4.12)$$

Here f is deformation potential in two level system model, W is the tunneling frequency given by $W=\omega_0 exp(\lambda)$, E is the tunneling splitting given by $E^2=\Delta^2+W^2$, ρ is the local sample density, $n(E,T)$ is the phonon occupation number defined as $n=(exp(E/kT)-1)^{-1}$, c is average speed of sound in the amorphous solid media and $\hbar$ is reduced Planck constant. Since W is usually much smaller than Δ , then $E \approx \Delta$. Using the tunneling prefactor Ω_0 we can rewrite the rate equations for uphill and downhill processes in a simpler manner:

$$R_{downhill} = \Omega_0 \exp(-2\lambda)(n(E,T)+1) \quad (4.13)$$

and

$$R_{uphill} = \Omega_0 \exp(-2\lambda)(n(E,T)) \quad (4.14)$$

Tunneling parameter λ is given by the Equation 3.1. The tunneling prefactor is also called attempt frequency, it is on the order of 10^{12} Hz. (See part 4.3)

In the previous parts it was mentioned that the lineshape of the spectral hole is Lorentzian and for small fractional hole depth $\Gamma_H = 2\Gamma_{\text{hom}}$. However, in practice the real measured hole width is affected by an additional factor Γ_{SD} that stands for Spectral Diffusion (SD), which is time and temperature dependent. Thus the realistic line width becomes:

$$\Gamma_H = 2\Gamma_{\text{hom}} + \Gamma_{SD} \quad (4.15)$$

Spectral diffusion occurs because of the conformational changes on the smallest barrier scale (see the bottom of the wells in Figure 4.9) of the energy landscape. The hole broadening and burning/recovery represent process on two distinct hierarchical tiers on the PEL. In the following we will focus on the evolution of spectral hole depth and area, not width.

4.4 Hole Growth Kinetics

Hole Growth Kinetics (HGK) technique is one of the most useful tools for TLS or energy Landscape Barrier parameters determination. In HGK experiments one investigates the growing of a spectral hole, or in other words the decrease of absorption or fluorescence excitation signal while the sample is illuminated. The fluorescence or transmission is monitored at burn wavelength continuously while the spectral hole is being burnt. The decrease of the fluorescence (or absorbance) signal usually is presented versus the irradiation dose. The burning is done with

constant (stabilized) power density. The signal is collected by the photomultiplier tube; however other photodetector options are possible. As the burnt molecules are no longer excited effectively and therefore do not fluoresce any more, the fluorescence signal should decrease in an exponential fashion. In practice, however, it cannot be fitted to a single-exponential curve because of the dispersion of the barrier parameters. To finalize the experiment one must compare the fractional depth of the scanned hole spectrum measured after the HGK is finished to the fractional hole depth resulting from the HGK measurement itself. The Hole Spectrum scanning is usually done with the intensities several orders of magnitude lower than the burning intensity and in the spectral region that is at least ten times wider the spectral hole width. This comparison allows to determine if the hole had any transient component that must be taken into account in the subsequent analysis.

This specific technique probes the parameters of the barriers in the excited state, since the key step of burning is the transition between substates in the excited state (recall figure 4.9). The parameters that are left free in the fitting and thus can be obtained include electron-phonon coupling (*S*), and the parameters of the distribution of the tunneling parameter lambda; for example, in the case this distribution is Gaussian - the tunneling parameter distribution mean (λ_0) and its standard deviation (σ_λ). To find the electron-phonon coupling parameter one should burn out all the resonant molecules (trough their ZPL) or in other worlds saturate the ZPH. The relation of the depth of the saturated hole (ZPH) to the electron-phonon coupling parameter *S* is given by Equation 4.20:

$$ZPLH \approx e^{-S} \quad (4.20)$$

Hole saturation (no more ZPL on this burning frequency are available) is manifested by a significant decrease in burning rate that is visible even on the logarithmic dose scale. After that the burning continues but very slowly, due to burning trough the PSB. To find the mean λ and σ_λ one has to fix all

the other parameters in the Master equation (4.8) to the values obtained independently from other experiments (e.g. PSB shape, PSB/ZPL ratio, fluorescence lifetime, etc.) and then to determine the best possible values for λ_0 and σ_λ of this HGK curve. Figure 4.10 shows the theoretical dependence of HGK curve on σ.

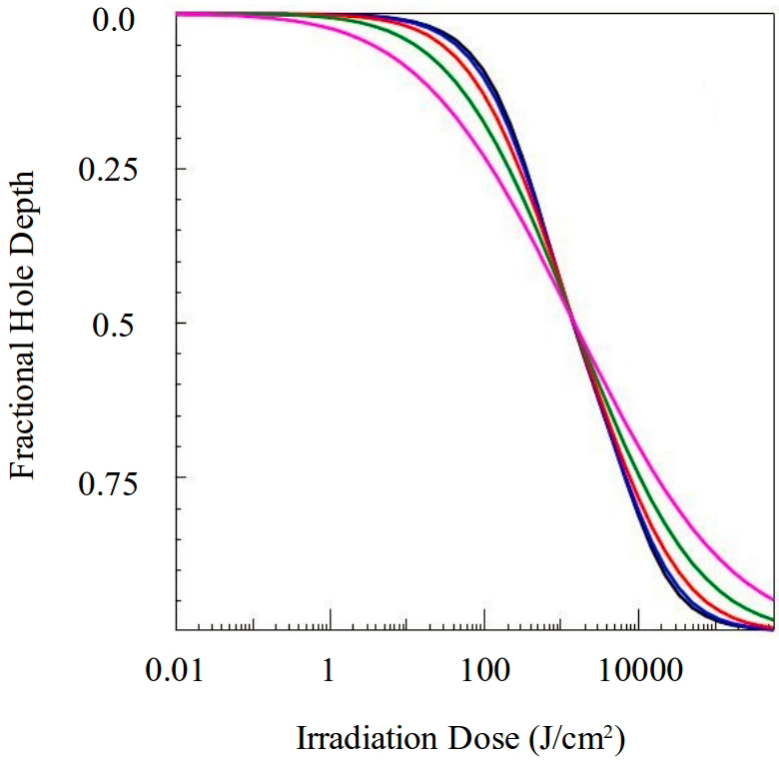

Figure.4.10: Modeled HGK curves for different parameters λ_0= 10 and σ_λ = 0.0 (no dispersion; black), 0.3, 0.6, 1.0 and 1.5 (magenta).

Here changing σ_λ leads to different curvature in HGK curve. The change in the mean of the λ_0 with all other parameters staying the same leads to shifting HGK curve towards higher or lower illumination doses without changing its shape. Figure 4.11

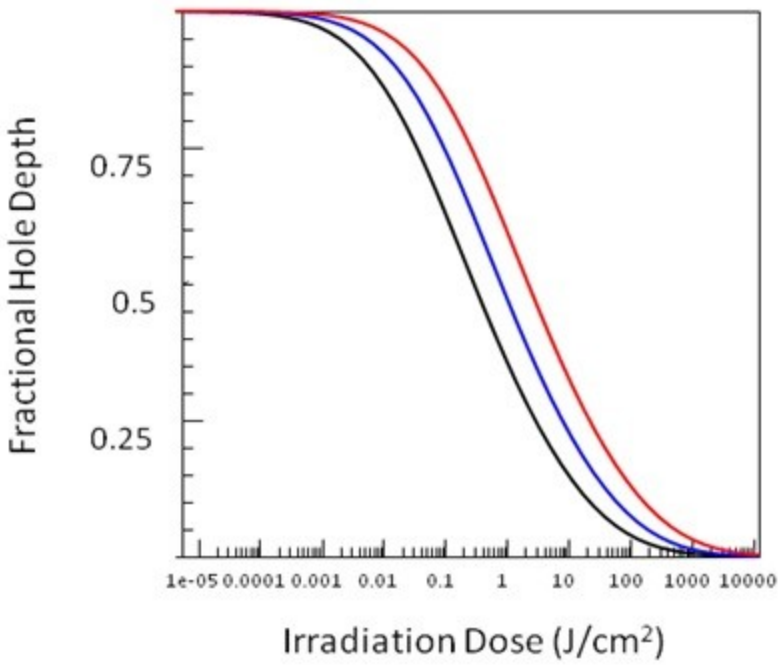

Figure 4.11: Simulated HGK curve at 5K with burn wavelength coinciding with the SDF peak. The Gaussian distribution of tunneling parameter λ_0 was peaked at various =11,10.5 and 10 for red, blue and black curves respectively. σ_λ=1.

4.5 Hole Recovery

Complementary to HGK technique which allowed for investigating the parameters of the excited state barriers, the Hole Recovery techniques gives the insights into the ground state barrier distributions. There are two types of hole recovery experiments that may be conducted. The first one explores hole recovery that occurs spontaneously at the same temperature as burning while the second one involves exploring recovery that is induced by the temporary increase of temperature.

HR at fixed temperatures. At fixed burn temperatures the recovery of the hole may take days, or even months, since this process occurs only through the tunnelling in the ground state (from

substate two to substate one in the TLS in Figure 4.9). It was shown by extensive modeling that full recovery of the hole does occur, but requires very long time.[12] The recovery expected within the first day is on the order of several tens of %. Full recovery occurs since the narrow spectral hole essentially represents a departure from thermodynamic equilibrium, and eventually the system will always reach equilibrium, it just may take very long time.

Thermocycling. Using this technique one should raise the temperature to the certain level (after the hole was burnt) and then temperature must be decreased back to the temperature of burning in order to measure the hole spectrum again. These steps are repeated with increasing the cycling temperature. During this process the recovery speeds up due to the heating of the sample and, as a result, by opening up the barrier hoping mechanism, while the tunnelling continues to contribute to recovery.

To analyze the hole recovery data we should determine the hole area as a function of time and of the history of changing the temperature. That is necessary for explanation of both spontaneous and thermocycling recovery. To carry out this analysis a number of assumptions should be made and additional quantities have to be introduced.

- The number of pigments in the burned and unburned states are N_0 and N respectively
- λ distribution in the ground state is $g(\lambda)$ (the distribution $f(\lambda)$ from the master equation (4.8) belongs to the excited state)
- The relaxation rate from burn to unburned state is $R(\lambda)$ at specific temperature T.

The number of recovered molecules that have relaxation rate between $R(\lambda)$ and $R(\lambda+d\lambda)$ is $N_0\, g(\lambda)d\lambda$ [23]. We can present the change in the number of the burned states as follows:

$$dN(t,T)=N_0 g(\lambda)d\lambda \exp(-R(\lambda)t) \quad (4.21)$$

where *t* is the recovery time. By integrating Eq. 4.21 over all possible λ the total number of unrecovered (that are still in the burned state) molecules is:

$$N(t,T) = N_0 \int_0^\infty g(\lambda) d\lambda \exp(-R(\lambda,T)t) \quad (4.22)$$

According to the previous studies [19, 23] the dominant process, as it was mentioned before, at low temperatures around 5K is tunneling. It follows from the near independence of the burning rates on temperature. Considering the tunneling rate we rely on (4.13) for downhill tunneling.[19] For thermocycling the rate of transition due to barrier hopping must be taken into consideration. The barrier hopping rate is determined by Equation 4.23:

$$R_{hopping} = \Omega_0 \exp(\frac{-V}{k_B T}) = \Omega_0 \exp(\frac{-\hbar^2 \lambda^2}{2md^2 k_B T}) \quad (4.23)$$

where Ω_0 is the attempt frequency and V is the potential barrier height which is expressed via λ, m and d by the Equation (3.1). The total relaxation rate may be written as a sum of 4.23 and 4.13.

Thus the overall rate of the relaxation including both mechanisms is:

$$R(\lambda,T) = \Omega_0 (n(E,T)+1) \exp(-2\lambda) + \Omega_0 \exp(\frac{-\hbar^2 \lambda^2}{2md^2 k_B T}) \quad (4.24)$$

Hence inclusion of both rates in to 4.22 for the thermocycling experiments yields:

$$N(t,T) = N_0 \int_0^\infty g(\lambda) d\lambda \exp(-\Omega_0 t[n(E,T)+1) \exp(-2\lambda) + \exp(\frac{-\hbar^2 \lambda^2}{2md^2 k_B T})]) \quad (4.25)$$

Or for the sake of simplicity:

$$N(t,T) = N_0 \int_0^{\infty} g(\lambda) q(\lambda,T,t) d\lambda \quad (4.26)$$

Where q is defined as:

$$q(\lambda,T,t) = \exp(-\Omega_0 t[(n(E,T)+1)\exp(-2\lambda) + \exp(\frac{-\hbar^2\lambda^2}{2md^2k_BT})]) \quad (4.27)$$

Function *q* shows how large is the fraction of unrecovered systems with specific λ after time *t* at temperature *T*. Since *q(λ, t, T)* is a step-like function, eq. 4.26 can be interpreted as follows: by multiplying *q(λ, t, T)* by the ground-state λ distribution *g(λ);* or, more precisely, the partial distribution encoded into the hole (see Figure 4.13), the smaller-lambda part of this distribution is chopped off, and the area remaining under the (partial) lambda-distribution curve, which is proportional to the hole area, is reduced (meaning the hole is partially recovered). Figure 4.12 shows the simplified visualisation of modifying the hole area by the *q*-function during the recovery.

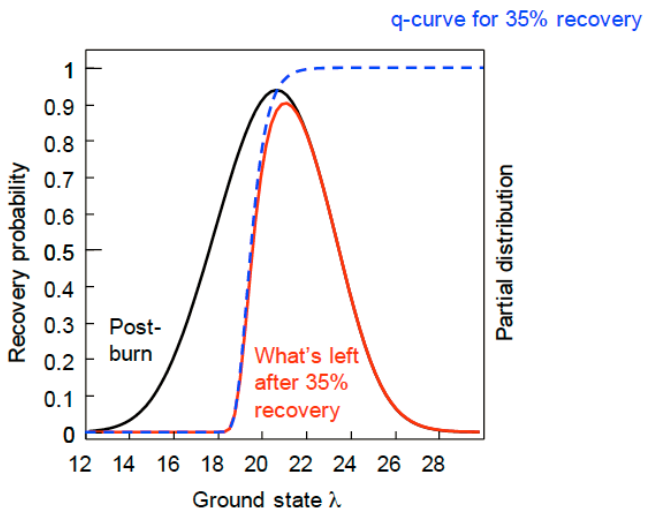

Figure 4.12: Post-burn partial _ distribution (black); q-curve resulting in 35% recovery of the hole (blue) and the partial distribution of lambda encoded into the remaining hole (red).

Figure 4.13 shows the examples of partial distributions encoded into the holes in the cases of Gaussian and Boxlike (uniform) barrier (or rather – lambda) full distribution (dashed lines), in the case when spectral memory (see below) is present. The distributions actually encoded in the holes (solid lines) are just (the lower-barrier) fractions of the full original distributions.

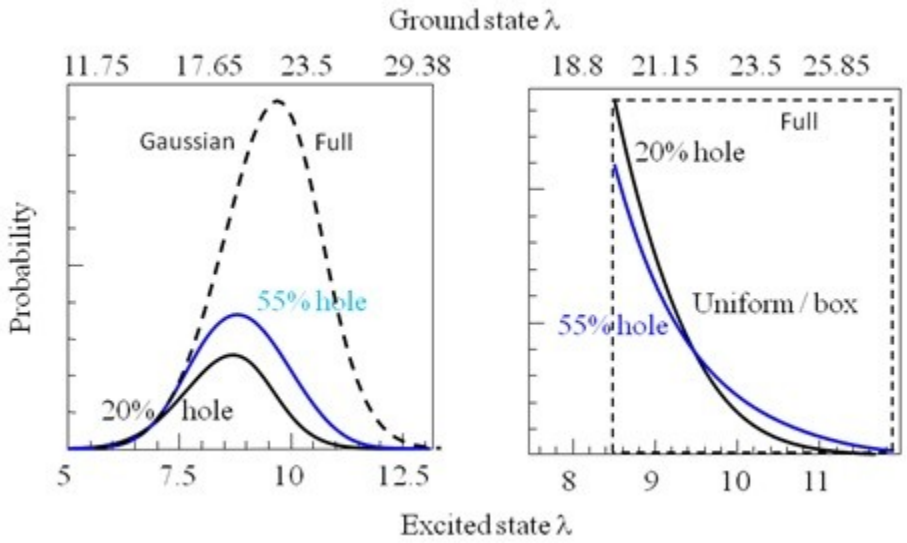

Figure 4.13: Partial distribution encoded in hole and reflected by hole recovery

In order to find out the distribution of the tunneling parameter in the ground state one should measure the hole area evolution with time, calculate $q(\lambda, t, T)$ and fit the experimental data to the Eq.4.26.

4.6 Fluorescence Line Narrowing

Fluorescence Line Narrowing is another line narrowing technique that is used to overcome the problem of inhomogeneously broadened absorption spectrum of a disordered solid. When using FLN only the resonant fraction of the inhomogeneously broadened absorption spectrum is

excited at low temperatures.[37]. Thus the collected fluorescence emission only belongs to the excited portion of the molecules. Therefore compared to conventional fluorescence spectrum.[38] the FLN spectrum is much narrower. Like the HB spectrum, the FLN spectrum also contains pseudo PSB and real PSB, however both of them are located to the red with respect to the ZPL / excitation frequency in contrast to SHB where the real PSB are to the blue of the ZPH.

In our studies we used Δ-FLN technique [39,40] which measures the difference between the FLN spectra before and after spectral hole burning. This technique is especially useful for defining the electron-phonon coupling parameters.[37] The main advantage of this technique is that the shape of the Δ-FLN is equal to the shape of the SSA spectrum since the double spectral selection effect of SHB and FLN effectively eliminates the pseudo PSB contribution.

Both SHB and FLN techniques provide independent information on the shape of the single-site spectrum. That is an important part of the model used in the study of energy landscapes of proteins (Master equation 4.8).

Chapter 5

Studying Protein Energy Landscapes

In this chapter we discuss the experimental results for Cyt b6f pigment-protein complex. The discussion is mostly based on the following paper:

- Probing Energy Landscapes of Cytochrome b_6f with Spectral Hole Burning: Effects of Deuterated Solvent and Detergent *Alexander Levenberg, Golia Shafiei, Maria A. Lujan, Steven Giannacopoulos, Rafael Picorel and Valter Zazubovich, Journal of Physical Chemistry B* 121 (2017) 9848–9858.

It will also include introductory data from previous work by Dr. Valter Zazubovich and his collaborators that is necessary to set the stage for our discussion. In addition, this work presents results from our latest experiments that will be included in a paper in preparation:

- Simultaneous Spectral Hole Burning Involving Two Tiers of the Protein Energy Landscape in Cytochrome b_6f. *Golia Shafiei, Alexander Levenberg, Maria A. Lujan, Rafael Picorel and Valter Zazubovich*

5.1 Introduction

For billions of years the photosynthesis process and its pigment protein complexes have served as molecular oxygen supplier and a perfect machine for conversation of sun energy into a chemical one. Today we have appropriate tools to study the energy landscape, conformational changes, energy transfer, as well as charge transfer and separation in these amazing complexes.

In our experiments we observe the dynamics of proteins by the means of optical spectroscopy. For the half of the last century optical experiments on amorphous solids were carried out by many researches to explore their dynamics and energy landscapes.[41,42,43] These experiments, which mainly rely on the theory of the impurity centers embedded in those solids, studied dynamics based on spectral line shifts induced by the light excitation. This information was inferred from Hole Growth Kinetics, and from Hole Recovery and Broadening at fixed temperatures or upon thermocycling. As it was mentioned before, SHB is a line narrowing technique, which helps to select pigments with similar ZPL out from the total population of the pigment molecules characterized by an inhomogeneously broadened spectrum. Laser excitation of this sub-ensemble may lead either to photo-chemical transformation of the molecules or to the conformational change in its protein surrounding (NPHB). At cryogenic temperatures in proteins the second process is by far more prevalent. The data observed during NPHB experiments provide us with the information needed for scrupulous analysis of shapes and parameters of the distributions of barriers and of the tunneling parameters. Moreover, the subsequent analysis may give the cue for a nature of so far unknown entities involved in the structural rearrangement.

Until recently, there were limited attempts at consistently interpreting different types of NPHB-related experiments as far as the shapes of the distributions were concerned. Hole growth kinetics (HGK) was modelled utilizing Gaussian distributions of the tunneling parameter λ for more than 20 years.[44-50] Occasionally, Gaussian λ-distributions for the ground state of the chromophore-amorphous host system were employed in fitting hole recovery or inferred from the interplay between burning and simultaneous recovery at elevated temperatures.[51,52] On the other hand, hole recovery upon thermocycling was usually reported without giving much details about the preceding burning (such as fractional hole depth), and with few exceptions

without attempting to determine not only the barrier (V) distributions, but also the λ-distributions or m or d.[49] More importantly, modeling of thermocycling results often required utilizing non-Gaussian barrier distributions.[53-55] Barrier distributions proportional to $1/\sqrt{V}$ yielding rectangular λ-distributions (uniform between certain λ_{min} and λ_{max}) follow from the theories of amorphous solids.[53-58] Gaussian distributions of λ, on the other hand, should yield only slightly asymmetric (as long as the mean of the λ–distribution is much larger than its width) chi-squared type barrier height distributions, not resembling those derived from the thermocycling results. [53-55]

Lately, single molecule spectroscopy, SMS (or single pigment-protein complex spectroscopy, SPCS) has become the technique of choice for studying spectral dynamics resulting from the dynamics of the amorphous hosts, including proteins. However, it must always be questioned which of the low-temperature phenomena observed in SMS or SPCS experiments are light-induced (i.e. are single-molecule acts of NPHB), and which are occurring anyway and are merely monitored by optical methods.[48] We believe that in the SPCS experiments by other groups the light-induced processes were for years erroneously interpreted as occurring anyway [48]. Thus, NPHB, utilizing much lower light intensities, is still capable of offering many valuable insights. Next question is if the barriers on the energy landscape are crossed via tunneling or thermally-activated hopping. SPCS experiments on LH2 complex suggested that both tunneling and barrier-hopping were responsible for the observed spectral dynamics.[60] Detailed understanding of light-induced small conformational changes in amorphous solids and proteins will be beneficial for interpreting both available and future SPCS results. Another interesting question pertaining specifically to pigment-protein complexes involved in light harvesting was raised in [61]– does introduction of additional energy to the pigment-protein

complex by exciting it via higher-energy pigments or excitonic states allow the environment of the lower-energy pigments to sample a larger set of conformational sub-states? Quantitative knowledge of the distributions of the barriers involved in NPHB and hole recovery will be critical for determining the degree of applicability of this idea to complexes featuring various donor-acceptor energy gaps.

The studies on CP43 complex in 2010 [19,24] showed, using both modes of the hole recovery (thermocycling and fixed-temperature) that the barrier distributions appear to be Gaussian. However for Cyt b_6f complex the same set of experiments results in mostly glass-like barrier distribution which can be interpreted as the direct "invasion" of glycerol/ water/ buffer matrix into the protein-pigment complex.[20] In the other words there is a concern for the intactness of our Cyt b_6f complex samples and if the observed dynamics does not belongs to the protein but to the glassy matrix. Another mechanism by which the pigment-protein complex is able to report on the dynamics of the surrounding glassy matrix is known as "slaving".

It is well known that spectral dynamics in many pigment-host systems is very sensitive to the exchange of protons for deuterons. (This is similar to a broader class of the phenomena where the rates of chemical reactions involving proton tunneling are strongly affected by deuteration.) In the cases when the pigment was in a direct contact with the deuterated hyperquenched amorphous water environment, the slowdown of NPHB by a factor of several hundred was observed, in agreement with the increase of the (mean of the distribution of) tunneling parameter λ from 8.0 to 11.2, i.e. by $\sqrt{2}$. [51] Fifteen-fold decrease of the NPHB yield was observed in $[Cr(oxalate)_3]^{3-}$ in ethylene glycol/water. [52] On the other hand, a massive increase of NPHB yield upon partial deuteration in $NaMgAl(oxalate)_3 \cdot 9H_2O$:Cr(III) was attributed to opening an additional NPHB channel involving flipping of the DOH molecules.[59]

Thus, here we will explore if deuterated environment affects the spectral dynamics of Cyt b_6f as well as that of Chl *a* in buffer-glycerol protein-free environment. In the process of exploring Cyt b_6f samples from different batches it also became evident that observed NPHB kinetics is fairly sensitive to the choice of the detergent used for sample preparation. This effect is also going to be examined.

5.2 Set up and Sample

Our group works closely with Dr. Rafael Picorel from Zaragoza, Spain, who has prepared the samples of Cyt b_6f. Chloroplastic Cyt b_6f was isolated from market spinach [21]. As cytochrome is originally a transmembrane protein, isolated cytochrome had to be solubilized with the help of a detergent. Two different types of detergent were used in samples employed in our experiments. For earlier ones reported in [2015] and for some additional experiments reported here we used n-octyl β-D-glucopyranoside (OGP) to disperse and stabilize the [protein complex in a micellar system]. [19] For the second batch we utilized *n*-dodecyl β-D-maltoside(DM), and sample purification was done as explained in [20]. Molar Extinction Coefficient of 25 $mM^{-1}\cdot cm^{-1}$ (at 554 nm), 21 $mM^{-1}\cdot cm^{-1}$ (at 563 nm), and 75 $mM^{-1}\cdot cm^{-1}$ (at 668.5 nm) were used for the Cyt f, Cyt b, and Chl, respectively to assess purity, quality and concentration of purified Cyt b_6f.[62.63] In our experiments we use glycerol-water-buffer to ensure formation of a transparent matrix at cryogenic temperatures and to protect the complexes. Some precaution was taken to carry out the experiments in deuterated environment to minimize possible exchange of the protein protons with deuterons, thus all samples were stored at $-80^{o}C$ and unfrozen only immediately prior to the experiment. For experiments on Cyt b_6f in deuterated environment we have purchased d_8-

glycerol (all protons exchanged) and D_2O from C/D/N Isotopes (Dorval, QC). To dissolve the pure Chl *a* (from Sigma-Aldrich) we used deuterated Methanol from C/N/D. Then we have dissolved <100 μL of methanol/ Chl *a in* ~1 mL of water-glycerol.

Figure 5.1 shows a cartoon of a Cyt b_6f complex surrounded by the detergent micelle in the solid (frozen) buffer-glycerol matrix.

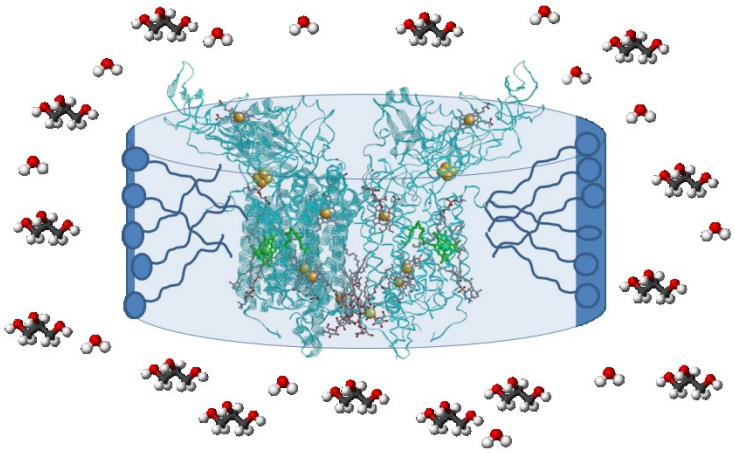

Figure 5.1: Cytochrome b_6f Complex solubilised with the help of detergent in water glycerol matrix.[8]

Absorption spectra were measured either with a Cary 5000 spectrophotometer with the resolution of 0.1 nm or with a home-built VIS-NIR spectrophotometer based on a Jobin-Yvon HR640 Single Grating Spectrograph with the bandwidth of about 0.04 nm**.** Broadband emission spectra were measured using Acton 2356 spectrograph with Princeton Instruments Pixis 1340x100 back-illuminated CCD. A 633 nm He-Ne laser was used for excitation. High-resolution spectra were measured with Sirah Matisse-DS frequency-stabilized tunable dye laser (bandwidth < 1 MHz). A 6 W 532 nm Spectra Physics Millennia was used as a pump laser. The samples were placed in a 4 by 10 mm cross-section plastic cuvette surrounded by an aluminum mask inside a liquid helium bath / flow cryostat (Ukrainian Academy of Sciences) with

temperature stabilized to better than 0.1 K. High-resolution experiments were performed in fluorescence excitation mode, with vertically polarized excitation and with fluorescence detected with a Hamamatsu photomultiplier / photon counting module at 90^{o} with respect to excitation. This ensures optimal collection of light emitted by the excited molecular dipoles. The intensity of the excitation light was stabilized by BEOC laser power controller (Brockton, MA) and regulated with absorptive neutral density filters. In experiments on Chl *a* in solution to ensure that monomeric chlorophyll was preferentially probed in fluorescence excitation mode, fluorescence was collected in the 695-710 nm range only. For Cyt b_6f the 700 nm long-pass filter was used in front of the PMT. Interference filters from Omega Filters (Bratelboro, VT) were employed.

5.3 Results

5.3.1 OGP Protonated Environment

HGK curves indicate the time or irradiation dose dependence of the fluorescence signal. It should be mentioned that the irradiation dose is defined as the product of constant laser intensity and the irradiation time itself. Since during this process the molecules cease to absorb at the fixed burning frequency, the fluorescence signal decreases. From our previous studies we have obtained [20] the Hole Growth Kinetics curves for Cyt b_6f in protonated environment (and OGP detergent micelle) sample shown in Figure 5.2

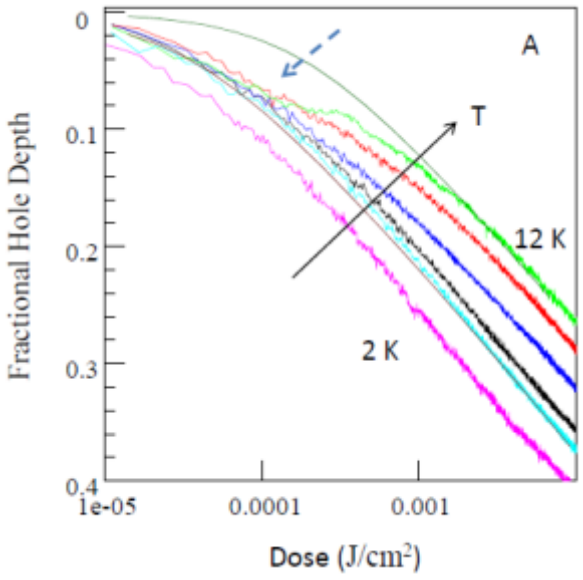

Figure 5.2: HGK curves for several temperatures from 2 K (magenta) to 12 K (light green). Dashed arrow indicates the region in the beginning of burning where by 10 K the burning is faster than tunneling-based model predicts (smooth green curve), likely due to burning via barrier-hopping. Also presented is the fit (smooth blue curve) to 5 K data (light blue). From [20]

Considering the general trends of HGK in the protein complexes one can conclude that with the increase of temperatures the rate of burning decreases as it shown on Figure 5.2. At the first glance this is surprising, since the rates of tunneling and especially barrier-hopping should increase with temperature. However, this decrease is in agreement with the increase of the homogeneous line width. Thus, the actual NPHB yield is almost independent on temperature, which proves that tunneling is the dominant NPHB mechanism. There is also some discrepancy in the beginning of the burning at elevated temperatures between modeled and experimental results which, most probably, is due to the onset of burning via barrier hopping in the excited state of the chlorophyll-protein system

Figure 5.3 reports on two thermocycling experiments with the protonated/OGP sample, both starting with the holes of 30% fractional depth, far from the saturated depth of about 50%. In the first experiment (black squares) the hole was allowed to recover at fixed temperature (~5 K) for an hour before thermocycling was initiated. Fast thermally-induced recovery step with the magnitude of about 15% of the original hole area is present in the temperature range around 11-15 K (left vertical arrow). In the second experiment (blue circles) the hole was allowed to recover at 5 K for ten hours before thermocycling was initiated. From the second to the tenth hours at 5 K the hole experienced significant additional recovery, comparable in magnitude to the 15% step described above.

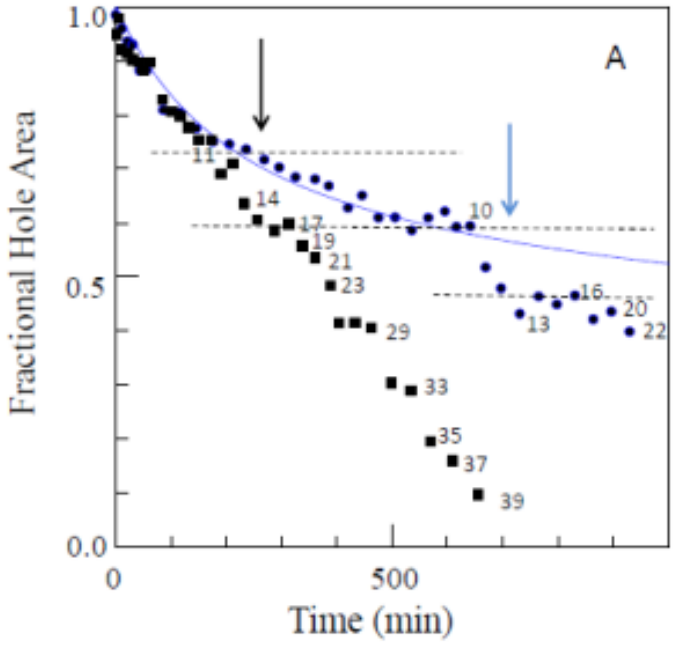

Figure 5.3: Recovery of a 30% hole with thermocycling started one hour (black squares) and ten hours (blue circles) after the end of burning. Solid blue curve is the fit to fixed-temperature recovery data. Vertical arrows indicate the fast recovery step at 11-15 K in two datasets. Horizontal dashed lines assist in estimating the magnitude of the step.

However, subsequent thermocycling still resulted in a recovery step at around 11-15 K (right vertical arrow), with approximately the same amplitude as in the previous experiment. This indicates that ten hours long recovery at 5 K did not include the respective systems, but these systems were easily accessible with a small temperature increase. Thus, there must be (at least) two distinct contributions to the hole burning and recovery, characterized by significantly different V and md^2 values, as opposed to a single-md^2 barrier distribution combined with reduced attempt frequency and mean of the λ-distribution that we proposed for Cyt b_6f earlier.[20] Figure 5.4 depicts, as a function of temperature, thermally activated fraction of the evolution of spectral holes that cannot be accounted for by the hole recovery of the same duration, but at 5 K.

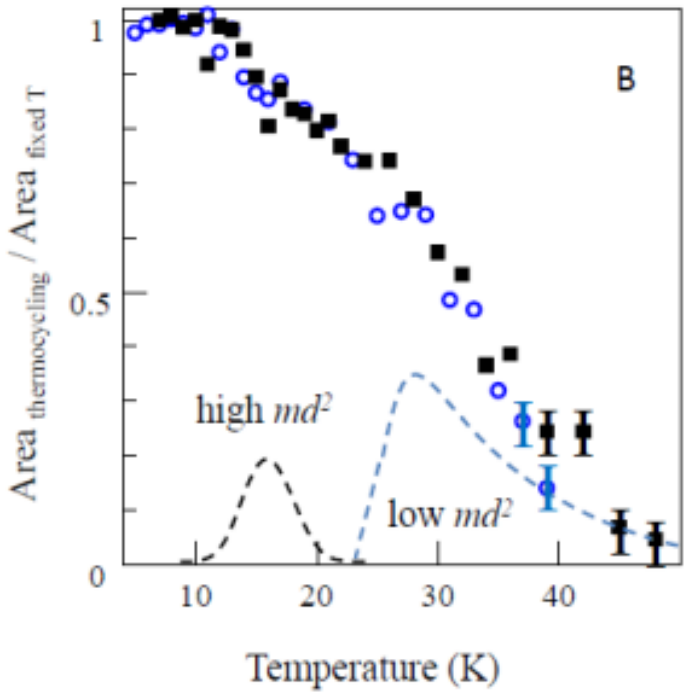

Figure 5.4: The first (black) dataset from Figure 5.3 represented as a function of temperature and a similar dataset from an independent similar experiment on deuterated sample (see below).

It is obtained by dividing the thermocycling data in Frame A (black squares in Figure 5.3) by the fit to fixed-temperature recovery (blue curve). It is a common practice to fit such data to determine the shape of the barrier distribution(s). However, more rigorous procedure must involve modeling data in Figure 2A while using the temperature change profile of the actual experiment. During the recovery the spectral holes evolve in such manner that λ-distributions encoded into the holes are multiplied by the q function (Eq. 4.27)

5.3.2 Deuteration effects in OGP-solubilized samples

Figure 5.5 shows the results of the experiments and also contains for comparison a 5.5K curve of the Cyt b_6f sample in protonated environment.

At the first glance it appears that based on fitting / modeling the 5 K HGK curves one can claim that in deuterated sample we observed the increase of the tunnelling parameter λ by about 8%, also the width of the λ–distribution increased somewhat. (Parameters used to obtain grey smooth curve in Figure 5.5 for the sample in protonated environment were fine-tuned somewhat with respect to Ref 20). However in the experiments with HGK with different intensities we observed the dependence of apparent burning rate on the illumination intensity in the deuterated environment samples. In Figure 5.6 several HGK curves are shown which were obtained at 5.5 K for Cyt b_6f in protonated and deuterated solvent environment and solubilized with OGP detergent. The protonated-environment sample curves in figure do not show much dependence on the intensity in the range that we have employed in these experiments while deuterated-environment sample demonstrates significant slowing down with the intensity increase. In figure

5.6 it is very difficult to see the pink curve of the protonated sample for the lowest intensity since it is almost invisible under the light blue, grey and red curves.

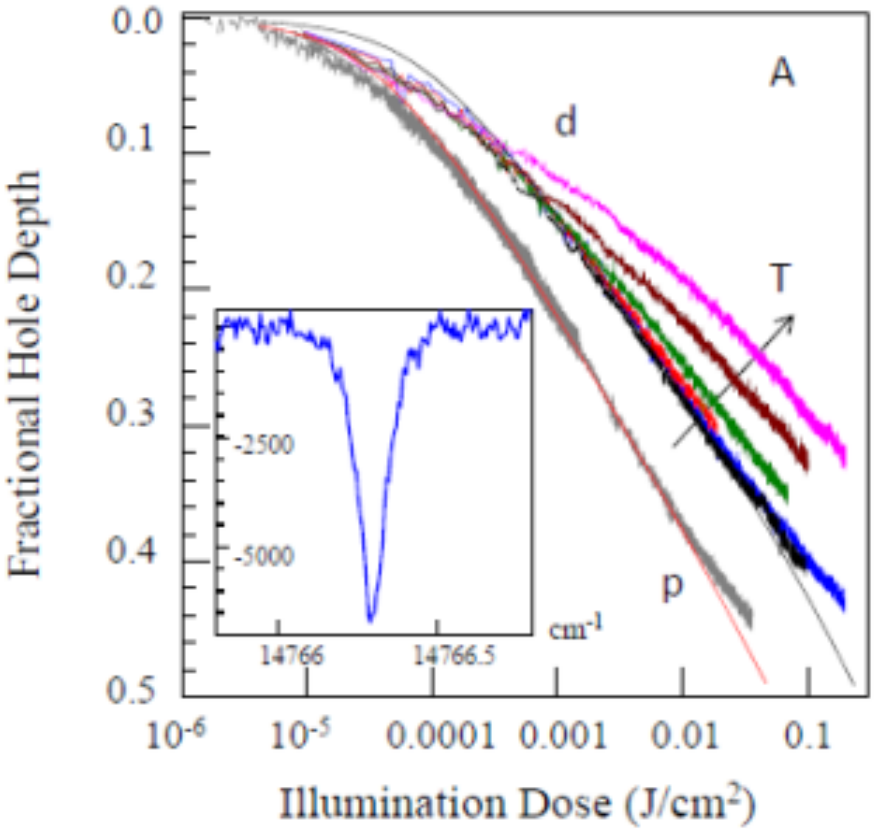

Figure 5.5: HGK curves obtained in OGP sample in deuterated environment at several temperatures from 5.5 K to 12.5 K. Grey curve is the 5.5 K curve for OGP sample in protonated environment and the same illumination intensity, 19 μW/cm2. Modeling results for 5.5 K HGK are presented as well (smooth red curve: λ=7.8…12.0, black curve: λ=8.2…13.1). The insert in Frame A contains an example of a 20%-deep hole measured in the sample featuring OGP detergent and deuterated solvent.

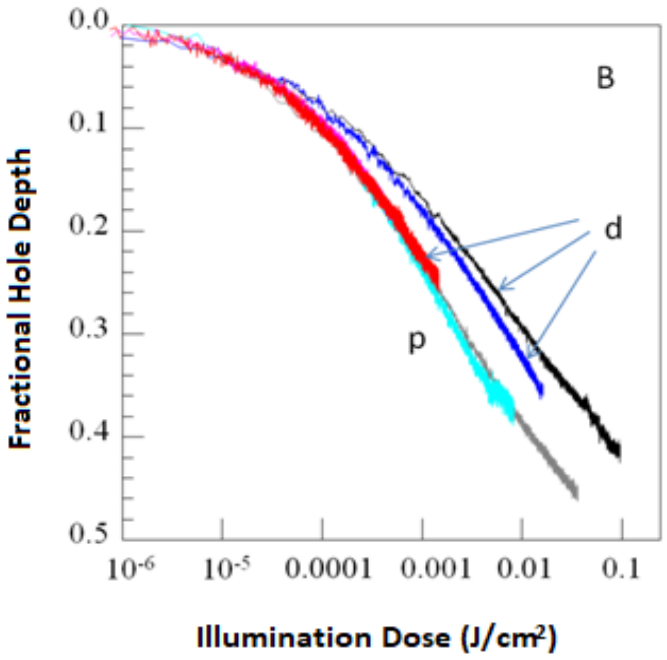

Figure 5.6: The 5.5 K HGK curves obtained for three different illumination intensities: Red -270 nW/cm^2, blue- 2.3 μW/cm^2 and black -19 μW/cm^2 for the deuterated Cyt b_6f sample. Pink, light blue, grey curves for the protonated sample. 0.001 J/cm^2 (corresponds to about 50 s with an illumination intensity of 19 μW/ cm^2)

For the sake of clarity I should mention that in Figure 5.5 we used the higher intensity curve of deuterated sample of 19 μW/cm^2 (Black curve). Therefore it is likely that curves presented in Figure 5.5 are influenced by this intensity effect.

The observation of hole recovery did not reveal significant deviations between protonated and deuterated-environment samples. Figure 5.7 presents data of protonated and deuterated OGP Cyt 6_bf samples, specifically the dependence of fractional hole area on the recovery time.

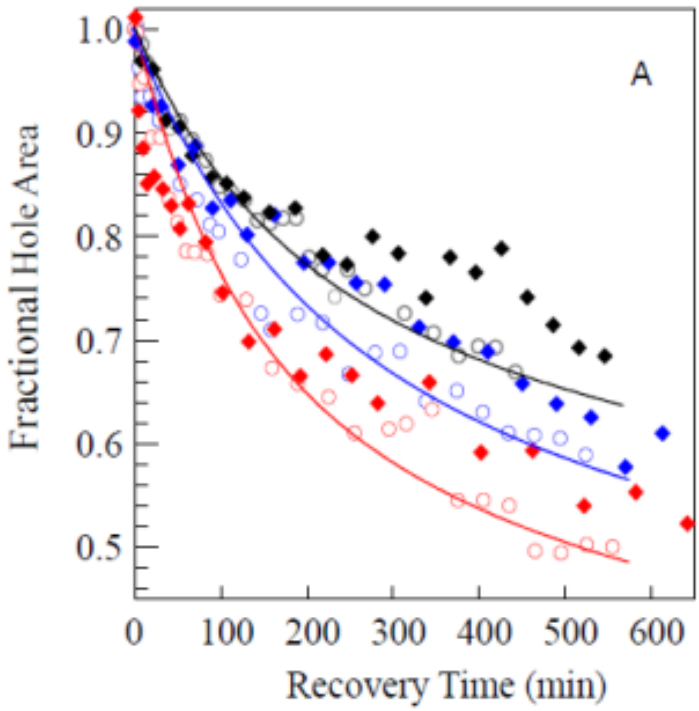

Figure 5.7: Recovery at fixed burn temperature for Cyt b_6f in regular/protonated (open circles) and deuterated (solid diamonds) environments. OGP sample. Red: 20%-deep holes, blue: 30% holes, Black: 40% holes.

We applied the same fitting parameters and the same logic as for the protonated environment Cyt b_6f complexes.[20] This strong similarity was observed at least for 10-12 first hours of hole recovery since longer recovery experiments were not conducted for deuterated samples. Thus the recovery data is still in better agreement with $1/\sqrt{V}$ barrier distribution shape than with the Gaussian one. The latter would result in a faster initial recovery and slower recovery at the later stages. The observed dependence of the rate of recovery on the fractional hole depth indicates the presence of a spectral memory mechanism, which is manifested by refilling of the spectral hole by previously burnt out molecules returning to their pre-burn transition frequencies but not by occasionally happening spectral diffusion. That, in fact justifies the use of TLS approximation.

Figure 5.8 presents selected data, only for 30%-deep holes, for protonated and deuterated samples in OGP micelles along with the fitting data. The recovery in deuterated samples is only slightly slower than for protonated environment. Thus one can suggest increase of tunneling parameter λ by about 0.8% for deuterated sample with respect to the protonated one. In Figure 5.8 also is shown short-dashed blue line depicting recovery expected if the tunneling entity were an –OH group, whose exchange for an –OD group would result in an increase of the ground state λ_g by 3%. We stress that tunneling parameter λ is present in the exponential in the equation for hole recovery, which makes recovery data extremely sensitive to even minor changes in λ and the mass of the tunneling entity m.

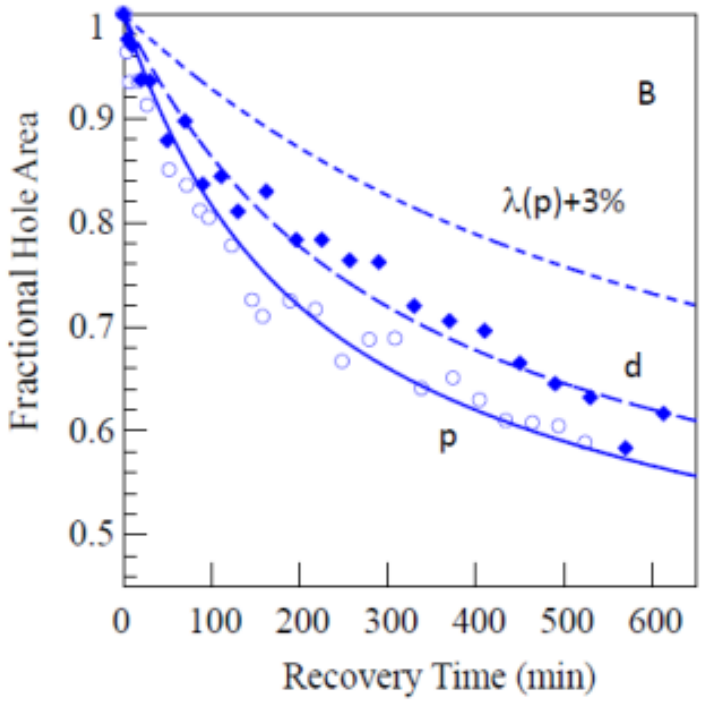

Figure 5.8: Recovery at fixed burn temperature for Cyt b_6f. Symbols and solid blue line are the same as in Figure 5.7. Long-dashed line represents the fit to the data for the deuterated OGP-based sample, corresponding to 0.8% increase of λ. Short-dashed blue line depicts recovery expected upon deuteration if the observed dynamics were due to –OH groups (increase of λ upon deuteration by 3%).

Comparing the increase of the ground-state λ_g by 0.8% in hole recovery experiments to the increase of 8% in tunneling parameter obtained from HGK curve (Figure 5.6), and also noticing that the difference in recovery data is comparable to the day-to-day variations observed in different experiments for the protonated-solvent OGP samples, we suggest that this 0.8% difference likely reflects either the imperfections of our experiments or minor real differences due to the differences in the sample's cooling history, for example. Hence, the hole recovery results not just exhibit near independence on deuteration, but also support the idea that the differences in HGK observed for protonated and deuterated OGP samples are not due to differences in the tunneling parameter.

We carried out a number of experiments using the thermocycling technique on Cyt6bf complexes with OGP detergent in deuterated environment. Figure 5.9 shows this data along with data for the fixed temperature recovery for the hole of the same fractional depth. The data depicted on Figure 5.9 contains two data sets of 30% deep spectral holes and the simulated hole recovery curve. The black square data set represents thermocycling-induced recovery where the numbers near some of the data points indicate the thermocycling temperature. The relative hole area is presented as a function of time rather than temperature. Originally these holes were burnt out at 5.5 K . Blue diamonds represent an experiment with hole (fixed temperature) recovery at this temperature. The thermocycling started from the same 5.5K and the hole recovery was completely finished by the time we reached 45 K. One can observe similar behaviour of both data sets below 11K, however above that temperature the thermocycling dataset starts deviating from the fixed-temperature one.

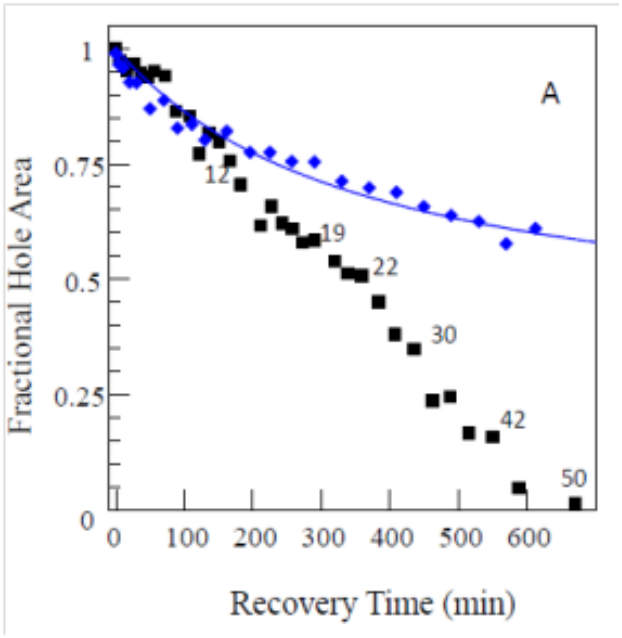

Figure 5.9: Thermocycling-induced recovery for Cyt b_6f in deuterated environment. OGP sample. Black squares: fractional hole area evolution upon thermocycling of a 30% hole. Cycling temperatures are indicated next to several datapoints. Blue diamonds: fixed-temperature recovery for a similar 30%-deep hole. Blue curve: simulated fixed-temperature recovery, same as in Figure 5.6 and 5.5

Figure 5.10 (repeating Figure 5.4) presents data on the part of the barrier distribution that cannot be accounted for by the fixed-temperature recovery for both deuterated and protonated OGP samples.

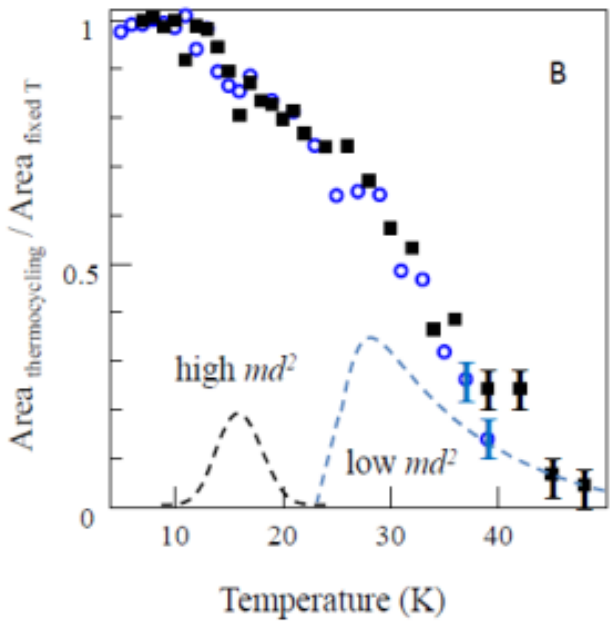

Figure 5.10: The (part of the) barrier distribution unaccounted for by the recovery at fixed burn temperature. Black squares: deuterated OGP sample. Open blue circles: protonated OGP sample. Dashed lines represent two components of the barrier distribution and are intended as a qualitative illustration only.

Here data is obtained by dividing of thermocycling data set to the simulated fit curve of recovery at fixed temperature. That dataset was presented in Figure 5.9 for deuterated environment sample. In the same manner we have obtained data for both protonated and deuterated samples. Thus the black squares dataset represents the λ distribution that did not take part in fixed temperature recovery (but has taken part in thermocycling) for deuterated sample and the blue one for a protonated sample.

To analyze this data one has to take into consideration that during the thermocycling we systematically let the sample stay at peak temperature of the cycle for one minute – $t_{max} \approx 60sec$, while T_{max} represents the peak temperature. In order to obtain the barrier distribution the data must be fitted with Eq :

$$f = 1 - \int_0^{T_{\max}} g(T)dT$$

Where *g(T)* stands for the distribution of barrier heights on temperature scale, and

$$V(T) = k_B T \ln(t_{\max}\Omega_0)$$

is barrier height on the energy scale. Taking attempt frequency of $7.6 \cdot 10^{12}$ GHz one gets $ln(\Omega_0 t_{max})$=33.75 and ground state barriers on the order of 1000 cm^{-1}.

Figure 5.10 also includes the schematic of two examples of two ground state barrier distribution components (dashed lines). These are intended for qualitative illustrative purposes only and are not meant to be perfectly consistent with all available experimental data. One may note that the left side of higher barrier distribution component is affected by preceding recovery which is manifested by modified shape of this component distribution. In other words, this is the distribution also affected by fixed burn temperature recovery. The information in Fig 5.10 seems to indicate that recovery in Cyt b_6f reflects a two-component distribution rather than one as was proposed in [20]. Detailed discussion on the interplay between these two components, their shape and parameters, the possibility of one barrier distribution with negative correlation between V and md^2, degree of "spectral memory", the possibility of competitive NPHB, etc, will be presented in the discussion section. At high cycling temperatures we add error bars to the experimental points to account for inaccuracies in hole area determination which are a result of hole broadening near the complete recovery.

As in the previous section there is no major difference between protonated OGP sample and the deuterated one. This is expected as the height of the barriers should not be affected by the deuteration process, yet it may result in the change of the mass of the entity which is about to make a transition.

5.3.3 Detergent Effects on Cyt b_6f complex

To explore the effect of the detergent on Cyt b_6f complex we performed a number of experiments. It must be mentioned that two batches differ not just by detergent, but also by the preparation method as it was explained in Setup and Sample section (5.2) [20,21]. Figure 5.11 shows the absorption and the broadband fluorescence spectra for OGP and DM based samples.

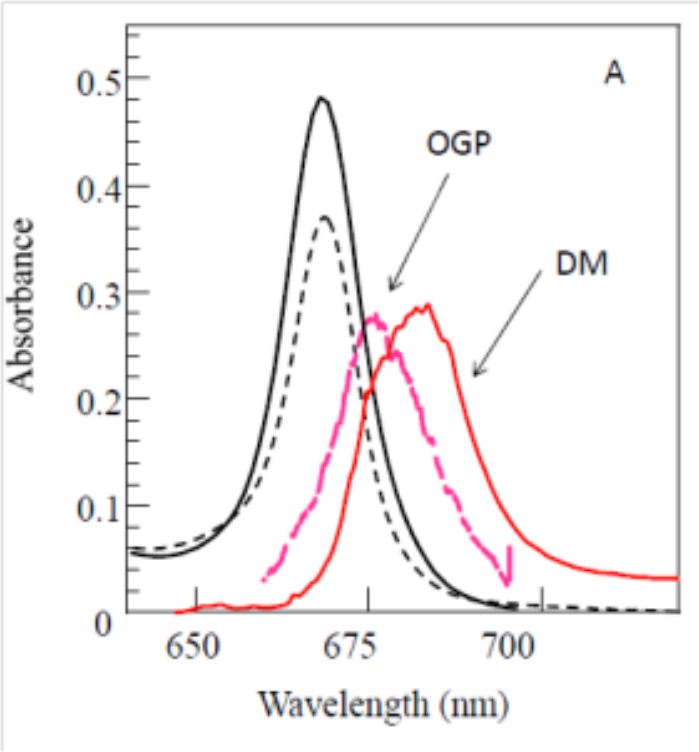

Figure 5.11: Absorption (black) and emission (red/pink) spectra of OGP (dashed line) and DM (solid line) based samples at 5 K. Emission was excited at 633 nm.

Comparing these two spectra one may note that qualitatively the results are similar for both batches, but the emission spectrum of the DM-based sample is red-shifted, while the absorption spectra have nearly identical shape.

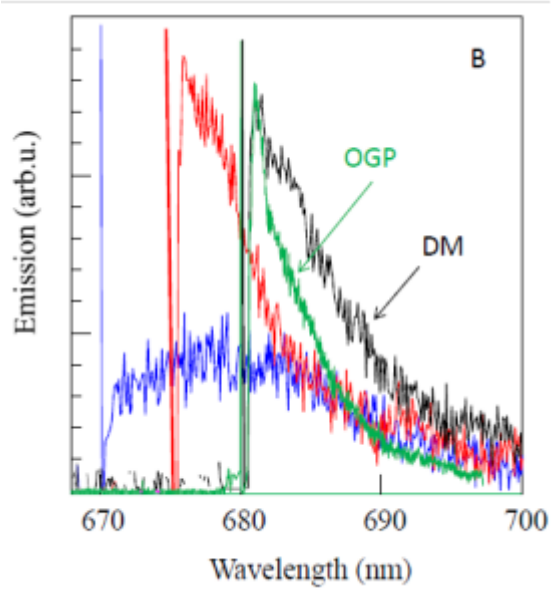

Figure 5.12: ΔFLN spectra for DM-based sample obtained with illumination at 670 nm (blue), 675 nm (red) and 680 nm (black). Green curve is the ΔFLN spectrum of the OGP-based sample, 680 nm excitation.

ΔFLN spectra of the DM sample are shown in Figure 5.12. ΔFLN spectrum of the OGP sample obtained with 680 nm excitation is shown for comparison. Strong red shift of the non-resonantly excited fluorescence, Figure 5.11 and the difference in the shape of the ΔFLN spectra, Figure 5.12, indicate significant increase of electron-phonon coupling in DM-solubilized samples. The ΔFLN spectrum for DM sample and 680 nm excitation (black) exhibits broader phonon sideband than the corresponding spectrum of the OGP sample (green), which is to be expected for higher electron-phonon coupling when multi-phonon processes are taken into account. (Also, ΔFLN spectra for 670 and 680 nm excitation are significantly different, which indicates the presence of energy transfer between the two chlorophylls of the dimer.) We were unable to burn more than 32% zero-phonon holes in the spectra of the DM-based sample, which indicates that Huang-Rhys factor *S* for phonons is about 1.1. According to modeling, increase of *S* from 0.72 (in OGP

samples) to 1.12 must result in about four-fold slowdown of spectral hole burning, if all other model parameters were staying the same.[20]

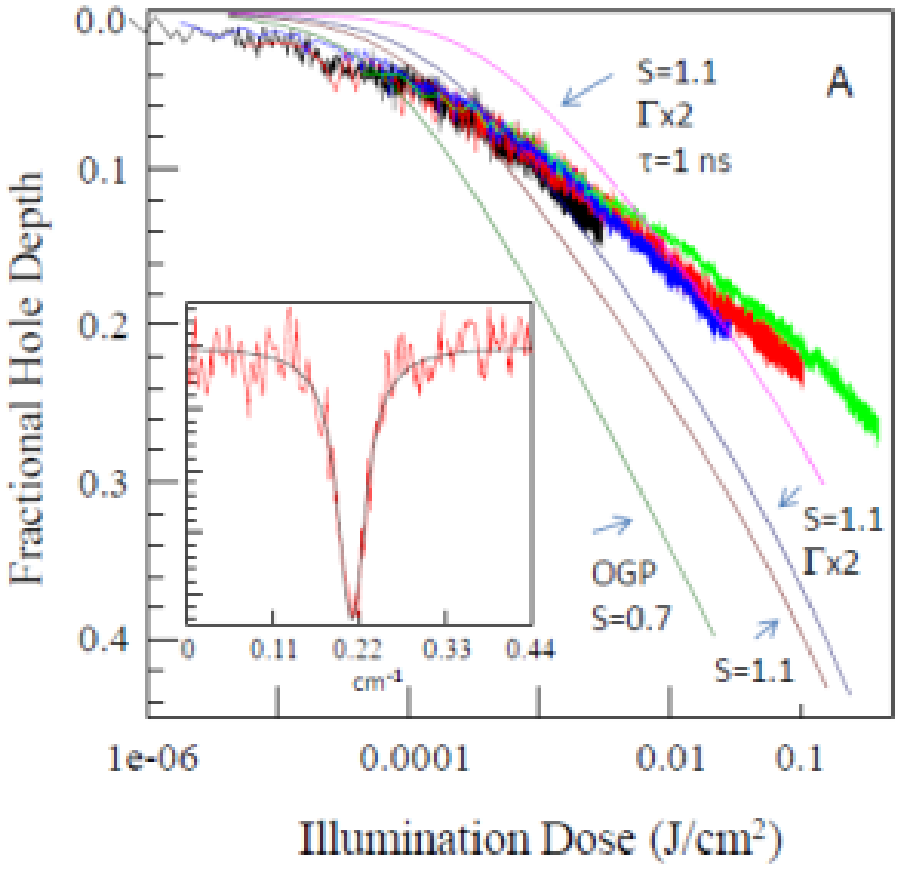

Figure 5.13: 5 K HGK curves for protonated solvent DM-based sample. The excitation intensities were 400 nW/cm^2, 3.5 μW/cm^2, 28 μW/cm^2 and 214 μW/cm^2 for black, blue, red and green curves, respectively. The insert in contains an example of a shallow hole at 2 K. Modeling details presented on this figure are discussed further.

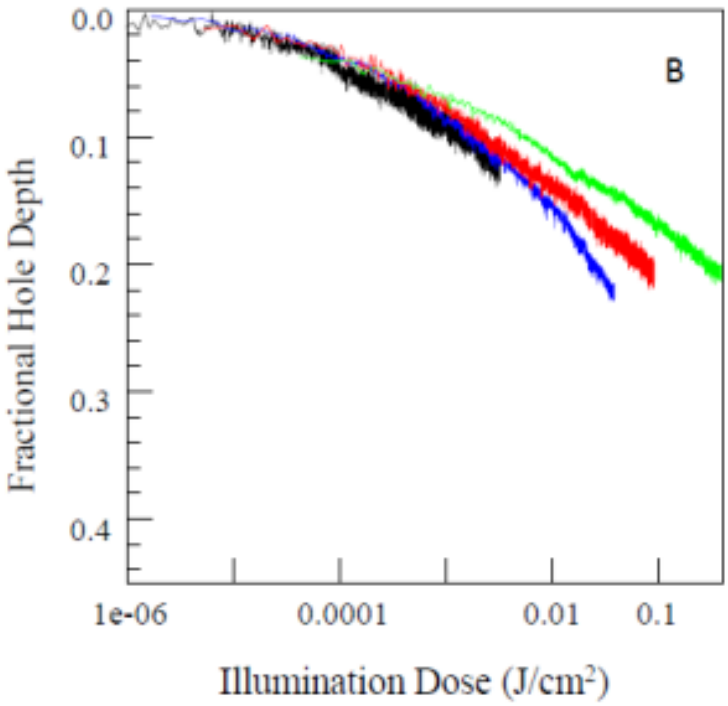

Figure 5.14 Same for deuterated DM-based sample. The excitation intensities were 400 nW/cm^2, 3.5 μW/cm^2, 28 μW/cm^2 and 214 μW/cm^2 for black, blue, red and green curves, respectively.

NPHB appears to be more than ten times slower in both protonated and deuterated versions of the DM-containing sample, Figure 5.13 and 5.14. (Note also the more pronounced intensity dependence of the HGK for deuterated sample, Figure 5.14. Thus, this effect is present regardless of the detergent micelle composition). Additional slowdown of burning could be explained by DM-based sample containing smaller fraction (or none) of Cyt b_6f with Chl a lifetimes not reduced by quenching by aromatic groups.[64] Note that DM was used as a detergent in Cyt b_6f samples where such quenching was previously reported.[80-82] Reduction of the lifetime from 2 ns to ~200 ps would easily explain ten-fold slowdown of burning, even without an increase of electron-phonon coupling (see Eq. 4.9). [80-82] The homogeneous line widths in DM sample were determined at several temperatures from 2 to 10 K and they were

systematically ~0.01 cm^{-1} (0.3 GHz) larger than those observed in OGP sample.[20] On the other hand, results obtained at 2 K are still suggesting lifetimes longer than 200 ps from [80-82]. Lifetime of 200 ps corresponds to the homogeneous line width of 0.0265 cm^{-1}. The narrowest linewidths observed for DM sample at 2 K are significantly, lower, about 0.0165 cm^{-1}. A 10%-deep 0.04 cm^{-1} wide hole (0.02 cm^{-1} line width, i.e. narrower than allowed by 200 ps lifetime) is shown in the insert in Figure 5.13. The 2 K line/hole widths still contain some contribution from pure dephasing, therefore 320 ps is just the shorter limit of the dephasing-free lifetime in our DM samples. Attributing the ~0.01 cm^{-1} difference between homogeneous line widths in OGP and DM samples to quenching, one can obtain the average quenching time of about 530 ps. Smooth dark green curve in Figure 5.13 represents a fit to the OGP sample data.[20] Smooth brown curve results from an increase of Huang-Rhys factor S from 0.72 to 1.12, all other model parameters staying the same. Smooth blue curve results from an additional two-fold increase of the homogeneous line width if this increase is attributed strictly to pure dephasing. Apparently, this is not enough. Some decrease of the dephasing-free lifetime (e. g. due to quenching) is required to explain the slowdown of burning without increasing the mean of the λ-distribution (smooth magenta curve corresponds to the decrease of τ_{fl} from 2.5 ns to 1 ns.). Experimental results in Figure 5.13 also suggest significantly broader distribution of NPHB rates than was observed for OGP-based sample and implied in above modeling. This increase could be attributed to either genuinely broader λ-distribution (but see the next paragraph) or to the distribution of the excited state lifetimes (in this case – quenching times). As demonstrated in [83], introduction of the line-width distribution indeed is expected to broaden the distribution of the NPHB yields.

The fixed-temperature hole recovery in DM-based sample is compared to the recovery in OGP-based sample in Figure 5.15.

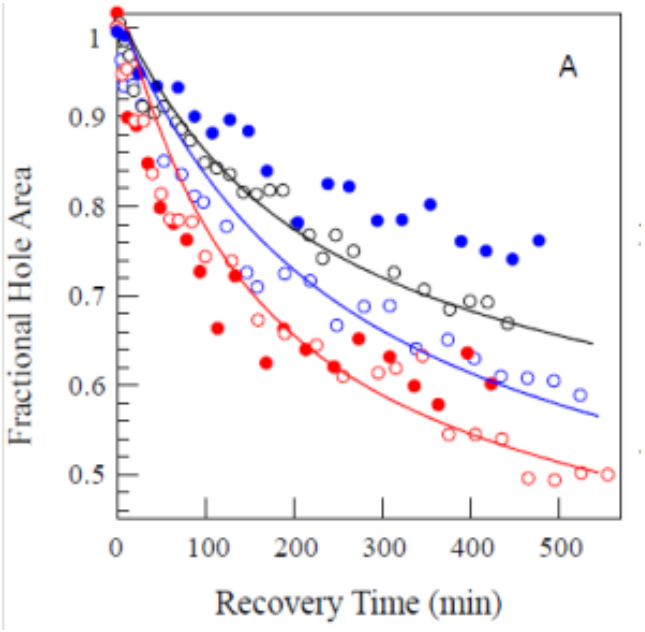

Figure 5.15: Fixed-temperature recovery of 20%-deep (red circles) and 30%-deep holes (blue circles) in DM-based sample, protonated solvent. Open circles show results for 20% (red), 30% (blue) and 40% (black) holes for OGP-based sample and respective simulated curves (solid lines). Red: 20% hole. Blue: 30% hole. Black: 40% hole.

The recovery of 20% holes proceeds at nearly identical rate in both samples. The recovery of a 30% hole was significantly slower in DM-based sample than in OGP-based sample. However, one should take into account that 30%-deep holes burnt into the spectra of DM sample (S~1.12) are much closer to saturation than 30%-deep and even 40%-deep holes for OGP-based sample (S~0.72) and consequently partial λ- (or barrier) distributions encoded into the holes have larger contributions from larger λ. (Assuming that one starts from the same true full barrier distributions prior to burning in all cases.) Thus, slowdown of the fixed-temperature recovery for nearly-saturated holes in DM-based samples is ultimately attributable to the increase

of electron-phonon coupling S and does not require any change in the full true barrier distribution before burning. The recovery of 30%-deep holes upon thermocycling was similar in protonated and deuterated DM-based samples. Figure 5.16 shows hole area as a function of cycling temperature, corrected for fixed-temperature recovery that would occur during the experiment.

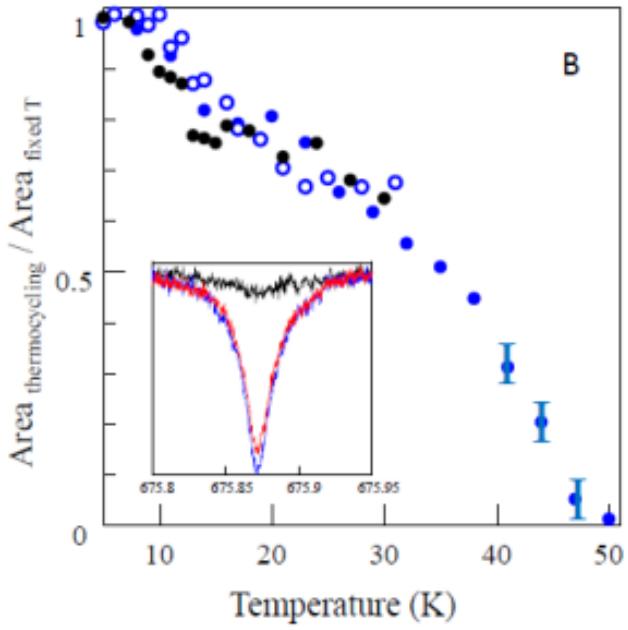

Figure 5.16: Hole area as a function of maximal cycle temperature in several DM-based samples, including deuterated one (black), 30% hole, protonated solvent. The insert shows examples of the hole spectra: first hole (blue); after one hour at 5 K (red) and after cycling to 41 K (black).

Thermocycling behavior of the DM-based samples was also similar to that of OGP-based samples (Figure 5.9) except that in the case of the DM-based sample some fraction of the hole persists till slightly higher temperatures. This is again expected if one remembers that 30% holes in DM-based sample are much more saturated than 30% holes in OGP-based sample and contain larger relative contribution from larger λ and V. The full distribution of the barrier

heights is unlikely affected by the choice of the detergent; these are the sub-distributions encoded into the hole that are different between OGP- and DM-based samples. Both protonated and deuterated DM-based samples feature a fast recovery step at around 11-15 K, just like OGP-based samples, indicating that two-component barrier distributions encoded into the holes is a general feature of Cyt b_6f, independent on detergent. The insert in Figure 5.16 contains examples of the hole spectra – right after burning (blue), after one hour of recovery at 5K (red) and after cycling to 41 K (black).

5.3.4 Chlorophyll in water / glycerol mixture

Since one of our greatest concerns was that we are obtaining the results for λ distribution that usually are presented by the glasses and polymers and that differ from what was observed in CP43 protein complexes, we conducted experiments to directly explore the dynamics of water-glycerol matrix and therefore hopefully exclude the possibilities of buffer invasion or of the protein dynamics slaving to that of the surrounding buffer-glycerol matrix. In order to explore the genuine dynamics of protein-free buffer-glycerol environment we placed the Chl a directly in the same host matrix which usually has been employed for dissolving our protein complexes. Since Chl is poorly soluble in water we dissolved it with small amount of methanol first, thus our solution (both protonated and deuterated versions) consisted of approximately over 30% water and over 60% glycerol, and the fraction of methanol was less than 10%. The absorption and emission spectra for both samples are shown in Figure 5.17.

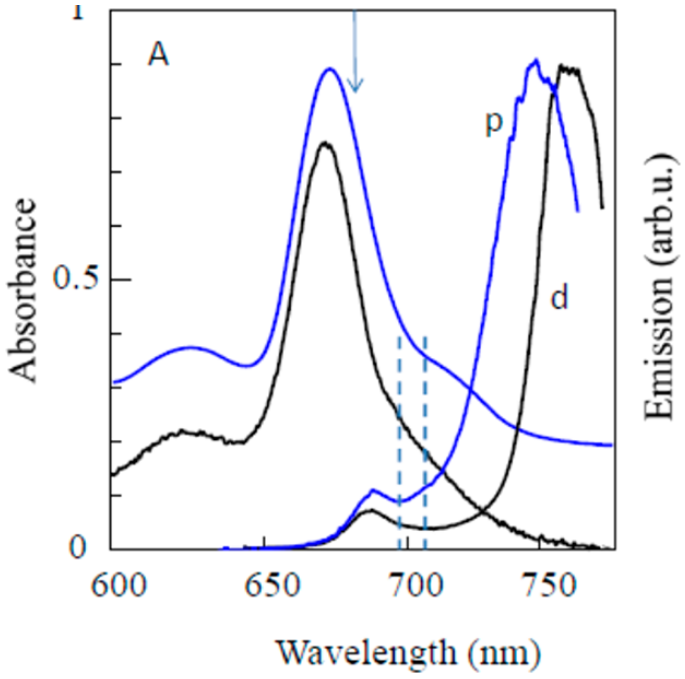

Figure 5.17: Representative absorption and emission spectra of Chl a in water/glycerol mixture with <10% methanol. Black: deuterated solvent. Blue: protonated solvent. The absorption spectrum of protonated sample is shifted up for clarity. Dashed vertical lines indicate the detection window for NPHB experiments in fluorescence excitation mode. The arrow indicates the hole-burning wavelength.

In the absorption spectra the main Q_y band is at about 670 nm and there is also a noticeable shoulder at 715 nm. The relative intensity of this shoulder gradually grows at the expense of the 670 nm band at room temperatures that in fact led us to conclude that this band is mostly because of the Chl aggregation. This is supported by the fact that at higher concentrations of Chl the relative intensity of 715 band was higher and that the sonication could at least partly reverse this process to increase the 670 nm band. These manifestations of aggregation of Chl are in a good agreement with those reported for 10% acetonitrile or DMF to 90%-water mixtures in [30]. However, we never observed absorption bands at ~740 nm as were reported in [31]. The aggregate absorption spectra are red-shifted due to excitonic coupling, in the same manner as in

many other system containing coupled pigment molecules [31]. Intense fluorescence is observed at 750-760 due to the presence of the aggregates, while the weak fluorescence of monomer is observed in the vicinity of 685 nm. In accordance to the data presented in Figure 5.17 one can recognize that the aggregated emission spectrum is strongly shifted with respect to absorbance, which indicates strong electron-phonon coupling and suggests that aggregates would not contribute much to the resonant NPHB (i.e. to zero-phonon holes).

The number of samples with different incubation times (including the samples that were left at room temperature for days) have been tested to ensure that the aggregation trend is in place. The spectra exhibited some variability in terms of peak positions and intensity ratios, however all of the samples showed aggregate fluorescence that was stronger than monomer fluorescence. Usually we observed higher peak in the absorption of monomer than for the aggregates shoulder, yet the emission spectra still provided us with higher fluorescence for an aggregated state. Thus, we suggest that water-glycerol matrix at low temperature quenches the monomeric fluorescence, in fact this is in good agreement with the data from [31] for Chl *a* in the mixtures of organic solvents and water at room temperatures. To probe monomeric Chl *a* selectively in fluorescence excitation mode, fluorescence was detected using 700-710 nm bandpass filter.

In order to understand if aggregation and quenching of the 680 nm fluorescence in water-glycerol Chl *a* solution are independent processes we performed a number of experiments with PVA gels. In these experiments Chl molecules were first trapped in the gel and then the gel was immersed into glycerol-water solution. After couple of hours the PVA gel was soaked with water and glycerol letting them to contact with the chlorophyll molecules. As a result the monomer Chl *a* fluorescence was heavily quenched but no aggregate fluorescence at 750 nm was observed, proving the independence of aggregation and quenching.

We performed NPHB in the Chl *a* monomer band to study the solvent dynamics, but NPHB appeared to be very inefficient in both protonated and deuterated samples. Figure 5.18

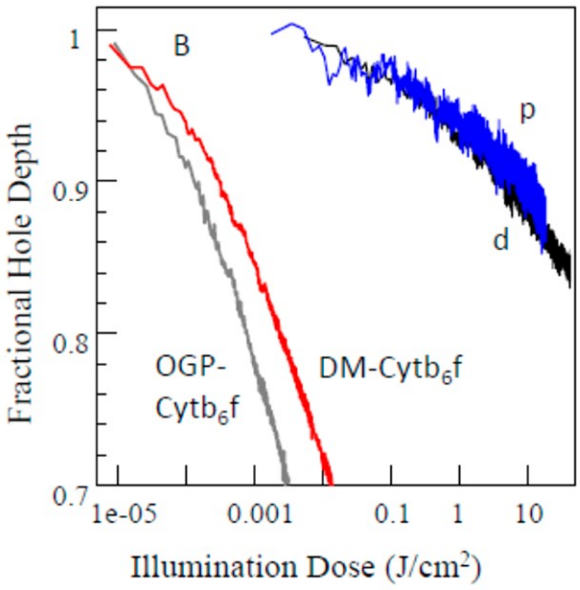

Figure 5.18: HGK curves for protonated (blue) and deuterated (black) solvent after correction for contributions from the long wavelength emission band within the detection window. Also shown, for comparison, are 5 K HGK curves for OGP (gray) and DM-based (red) Cyt b_6f samples.

We managed to reach the hole depths of at most 10% with burning for couple of hours at very high intensity. For comparison in Figure 5.18 we show the HGK curves for two batches of Cyt b_6f with OGP and DM detergent. Here the light intensity for Chl burning is about 4 mW/cm^2 which is approximately 200 times higher than was needed for samples of OGP-solubilized Cyt b_6f to be burnt to 30% of fractional hole depth, and 20 times higher than in Figures 5.13 and 5.14 for DM-solubilized cytochrome sample. We did not continue these experiments much further due to poor fluorescence and NPHB yields and signal to noise ratio, yet we still were able to draw a conclusion based on the lack of difference between the protonated and deuterated

samples. In all experiments deuterated samples exhibited even somewhat faster burning than protonated ones. This, however, was most likely due to different contributions of the shorter-wavelength tail of the aggregate fluorescence to the total fluorescence within the detection window since the aggregate fluorescence peak in protonated sample was at somewhat shorter wavelength. Therefore we can suggest that about half of the fluorescence in the 695-710 nm detection window in protonated samples belongs to the monomers. Thus, deuteration does not significantly slow down the NPHB process in chlorophyll in water / glycerol mixtures. This, in turn strongly suggests that single protons are not the entities responsible for the spectral dynamics in water-glycerol mixture. The precision of these measurements is insufficient to confirm or disprove any -OH group dynamics.

5.4 Discussion

5.4.1 Nature of the Tunneling Entities.

Fitting various recovery results using one single barrier or λ–distribution as suggested in [20] ultimately proved impossible. Thus, spectral hole burning in Cyt b_6f may involve two tiers of the protein energy landscape featuring degenerate distributions of the NPHB yields (or excited-state λ in case of similar attempt frequencies), with similar yields resulting from different combinations of md^2 and V (see for example Figure 5.10). (At the moment we cannot exclude an alternative scenario involving one energy landscape tier with negatively correlated barrier and md^2 distributions. While simple TLS model in Figure 4.9 provides no reasons for such a correlation, the presence of a distribution of md^2 values for the same tier of the energy landscape would point to cooperative effects. The numerical values for md^2 reported below would then represent the limits of the range of possible md^2 values). The data from the thermocycling experiment following ten hours of fixed-temperature recovery (Figure 5.3 and 5.4) can be used for estimating md^2 for the energy landscape tier responsible for the 11-15 K step in the following way: Consider that one minute at, let's say, 12 K had larger effect on the sub-distribution of barriers responsible for this recovery step than 600 minutes of recovery at 5 K and thus, independently of the attempt frequency, $600\,\mathrm{min}\cdot\exp(-2\lambda_{gr}) \le 1\,\mathrm{min}\cdot\exp(-\lambda_{gr}{}^2\hbar^2/2md^2k_B 12K)$ (In WKB approximation, with rectangular barriers.) Equality corresponds to a situation when after ten hours of recovery at 5 K the q-curve, moving towards the larger $\lambda_{gr,}$ has reached exactly $\lambda_{gr,\,min}$ of this sub-distribution. Solving the above equation results in the lower limit of $md^2 > 2.1\cdot10^{-46}$ kg·m^2 for the "black" component (from the determinant of the quadratic equation

for λ). This small value of md^2, however, corresponds to $\lambda_{gr,\,min} \sim 6$, which would require even more drastic reduction of the attempt frequency than was proposed in [20]. We will return to this discussion shortly.

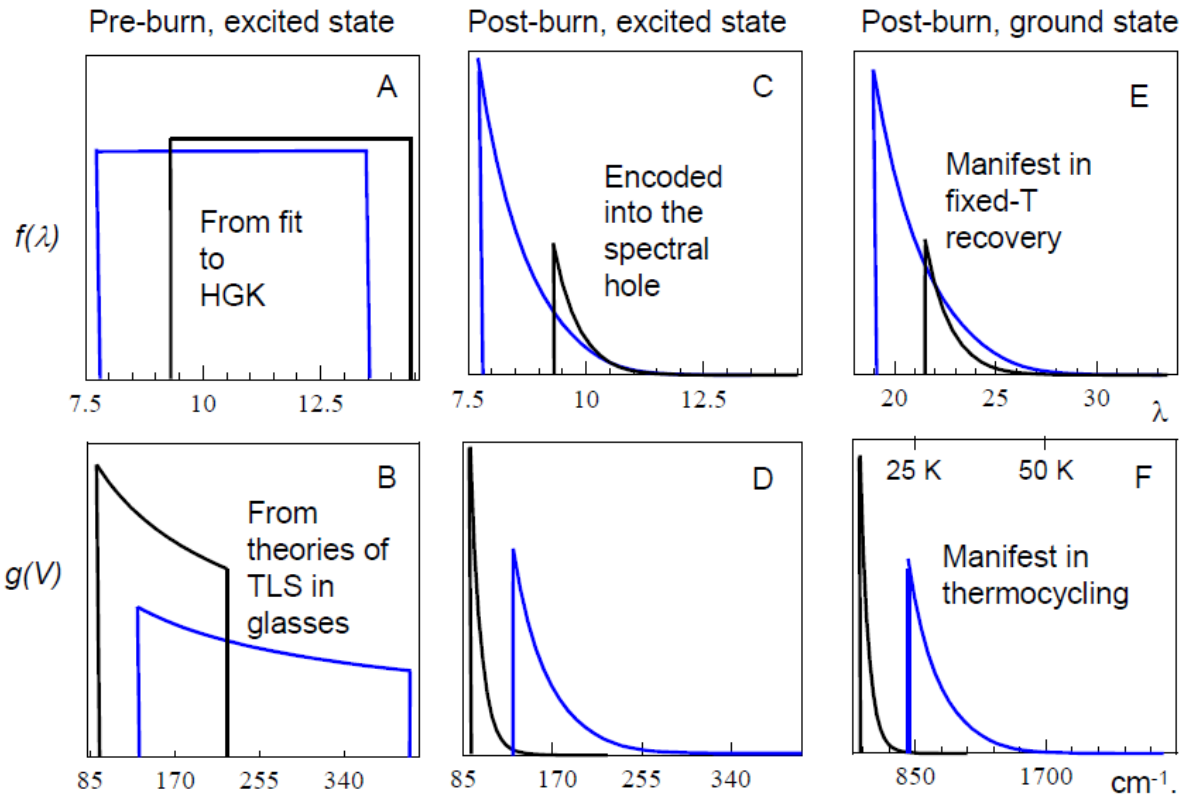

Figure 5.19. Likely relationship between two distributions (and sub-distributions encoded into the holes) affecting spectral hole burning and hole recovery in Cyt b_6f. Frames A and B depict full true λ-distributions and barrier distributions, respectively while frames C-F represent partial distributions encoded into the holes. The true full pre-burn distributions for the ground state would look like A and B but with the horizontal scale from E and F, respectively. Blue: lower md^2 higher-V component. Black: higher md^2 lower-V component. Note the switch between "blue" and "black" components between upper and lower rows of the figure.

Figure 5.19 introduces the two-component model following from the data in Figure 5.3, 5.4 and 5.10. NPHB is simultaneously (and perhaps competitively, see below) probing two distinct barrier distributions with two different generalized coordinates and with overlapping

ranges of NPHB yields (combinations of excited-state λ and Ω_0) – one with lower barriers V and higher md^2 (black) and the other with lower md^2 and higher V (blue). The lower md^2 higher V tier (blue) may feature either systematically higher values of NPHB yield (i.e. lower λ, as shown in Figure 5.19) or just broader NPHB yield distribution ensuring that the lower-λ end of the combined distribution features lower md^2 and thus there is no significant burning by barrier-hopping in the excited state at 5 K. In thermocycling experiments the lower-barrier higher-md^2 part (black) is the first to recover (note the switching of the black and the blue curves between parts A, C, E and B, D, F of Figure 5.19).

Another conclusion that can be made comparing thermocycling and fixed-temperature recovery data in view of Figure 5.19 is that $k=\lambda_{gr}/\lambda_{exc}$ should not be significantly smaller for the "black" tier than for the "blue" tier: If there were more overlap between the two ground-state λ-distributions (imagine shifting black curve in Figure 5.19E even more to the left, current figure has k_{blue}=2.42 and k_{black}=2.31, see below), both "blue" and "black" tiers of the landscape would contribute significantly to the tunneling-dominated fixed-temperature recovery at earlier times, and by 10 hours significant portion of this "black" component would be recovered.

Before engaging in further modeling, one has to narrow down the range of possible qualitatively different options. Given the uncertainties of the data in Figure 5.4 or 5.10, three different scenarios involving two barrier distributions are possible based on thermocycling data alone:

(a) Some narrow distribution for about 15% of the total hole area (explaining the 11-15 K recovery step), plus broad distribution descendent from a Gaussian one and peaked at around 33 K;

(b) Broad distribution descendent from $\sim 1/\sqrt{V}$ and covering almost the whole temperature range, plus overlapping narrower Gaussian distribution peaked at around 27-28 K; and

(c) Two distributions descendent from $\sim 1/\sqrt{V}$ and covering temperature ranges from 10 K to about 25 K (about 25% of the total hole area) and from 25 K to 50 K, respectively.

Note that in all of these scenarios the sub-distributions for "blue" or perhaps both components are modified by fixed-temperature recovery before thermocycling. Scenario (a) is incompatible with fixed-temperature recovery data indicating that the distribution predominantly encoded into the hole is descendent from the $1/\sqrt{V}$ distribution. Scenario (b) closely resembles that reported in [55]. However, in this scenario once we require that fixed temperature recovery is dominated by a component descendent from the $1/\sqrt{V}$ distribution, this same component becomes responsible for both initial fixed-temperature recovery and the first significant recovery step upon thermocycling, defying the logic of Figure 5.19. Thus, scenario (c) is in the best agreement with the available data, at least on a qualitative level.

Next question is if the NPHB involving two tiers of the protein energy landscape is competitive (both channels are simultaneously available for the same system) or if two NPHB channels are mutually exclusive. Modeling of the latter case involves simply a weighted sum of burning and recovery processes for two overlapping absorption bands with different md^2. The competitive NPHB on two different tiers of the protein energy landscape can be modeled assuming that NPHB yields for two competing hole burning processes will be

$$\phi_1(\lambda_1,\lambda_2)=\frac{\Omega_{01}\exp(-2\lambda_1)}{\Omega_{01}\exp(-2\lambda_1)+\Omega_{02}\exp(-2\lambda_2)+\tau_1^{-1}};$$

$$\phi_2(\lambda_1,\lambda_2)=\frac{\Omega_{02}\exp(-2\lambda_2)}{\Omega_{02}\exp(-2\lambda_1)+\Omega_{02}\exp(-2\lambda_2)+\tau_1^{-1}}$$

where Ω_0 is the attempt frequency, determining how often the systems try to cross the barrier between the two wells, and τ_1 is the fluorescence lifetime. The total NPHB yield will be $\phi(\lambda_1,\lambda_2) = \phi_1+\phi_2$. Contributions of two tiers of the energy landscape to any spectral hole at the end of the burning would scale as ϕ_1 *to* ϕ_2.

In order to determine if the competitive burning approach is capable of explaining our observations, we attempted modeling HGK, recovery and thermocycling data in Figures 5.2, 5.3 and 5.4. First, the HGK data was fitted in order to determine possible ranges of λ for two distribution components in the excited state. As long as λ_{min} of the additional landscape tier (black) is significantly larger than λ_{min} of the first one (blue), the presence of the second burn channel does not affect the beginning of the burning, dominated by the smallest λ. As the depth of the hole increases, contributions to burning from two tiers of the energy landscape may become comparable. Thus, HGK curves behave as in the case of a single-component λ-distribution with much smaller width. For instance, reasonable fit to 5 K HGK curve in Figure 5.2 can be produced with a combination of two box-like λ–distributions, one ranging from 7.7 to 13.5 and another ranging from 9.3 to 14.5. The first (blue) distribution is significantly broader than a single distribution that was required for fitting the same HGK curve (7.8 to 12.0, i.e. 4.2 units versus 5.8 above). Two partial distributions produced with the above parameters as the starting point and encoded into the 30% holes are shown in Figure 5.19C. These partial distributions are probed in the recovery experiments, not the full ones in Figure 5.19A. The area

under the black curve is about 17% of the total area under both curves combined. Two-component model offers even slightly better fit to the fixed-temperature recovery data, especially at long times, and yields $k=\lambda_{gr}/\lambda_{exc}$=2.42. With k =2.42 the lower-barrier distribution (black) features md^2 of about $5\cdot10^{-46}$ kg·m^2. However, there is no reason why different tiers of the energy landscape should feature exactly identical $k=\lambda_{gr}/\lambda_{exc}$. This is just an empirical constant. As "black" component is not manifesting in fixed-temperature recovery experiments within reasonable time, it is not possible to determine its md^2 by directly comparing fixed-temperature recovery and thermocycling data as in [49] Instead, one can determine the likely range of pairs of k and md^2 for this landscape tier. The range of reasonable k and md^2 is limited from above by the requirement that barrier-hopping should not contribute much to the initial stages of NPHB at 5 K and from below by $2.1\cdot10^{-46}$ kg·m^2 (see above). In fact, $md^2 = 5\cdot10^{-46}$ kg·m^2 already implies much more barrier-hopping than tunneling at 5 K for $\lambda_{min,\ exc}$=9.6 of the "black" component. $\exp(-\lambda^2\hbar^2/2md^2k_BT)/\exp(-2\lambda)\sim 180$. Setting barrier-hopping and tunneling rates at 5 K to be equal for $\lambda_{min,\ exc}$=9.6 one gets $md^2 \sim 3.85\cdot10^{-46}$ kg·m^2 which might be a more realistic estimate for this tier. This in turn would require k= 2.12. The problem with this line of reasoning is that even a small contribution of high md^2 systems would make burning at temperatures higher than 5 K too fast. And for $k=\lambda_{gr}/\lambda_{exc}$=2.12 the "black" component should be significantly recovered during the first 10 hours and the q-curve would reach that value in 8 hours.

For thermocycling the lower-barrier higher md^2 part is the first to recover. This component features md^2 of about $4\cdot10^{-46}$ kg·m^2 as can be determined from the modeling of the fast recovery step observed in thermocycling experiments at 11-15 K (Figure 5.9,5.10). This value is too large to be ascribed to the tunneling of a single proton in a double-well potential associated with a hydrogen bond in either the protein or glassy solid surrounding protein. We

note that a "photoconversion" hole burning mechanism involving rearrangement of a hydrogen bond between protein and chlorophyll was proposed in the core antenna complexes of Photosystem II.[65.66.67] For a single methyl or hydroxyl group $md^2 \sim 4 \cdot 10^{-46}$ kg·m^2 would mean a displacement d of ~1 Å. The md^2 value for the second component, dominating fixed-temperature recovery ("blue"), could be inferred from thermocycling data for higher temperatures and the data on the very beginning of the NPHB process in Figure 5.5 that suggests $md^2 \approx 1.5 \cdot 10^{-46}$ kg·m^2 for systems involved in the initial hole burning and featuring the lowest λ_{exc}. Relatively high value of md^2 would effectively rule out the tunneling of a single proton in a double-well potential associated with a particular hydrogen bond as a possible source of the dynamics represented by the blue curve as well. The expected md^2 in this case would be significantly lower than $1.0 \cdot 10^{-46}$ kg m^2, taking into account that separation of the potential wells in this scenario is smaller than the hydrogen bond length. Cooperative effects involving the whole hydrogen bonds networks of the protein are still possible, since in this case m becomes uncoupled from the mass of some one particular atom or chemical group.

HGK and recovery results obtained for Cyt b_6f in deuterated buffer / glycerol environment indicate almost no deuteration effects. This clearly rules out the possibility that any spectral dynamics is due to proton / deuteron tunneling in the outside solvent, including the scenarios involving cooperative effects. Since $\lambda \sim \sqrt{m}$, increasing m by a factor of two would result in an increase of λ by a factor of $\sqrt{2}$. Depending on the range of λ (different combinations of matching λ and attempt frequency Ω_0 would produce the same HGK curves, (see Eq. 4.9), the NPHB yield and fixed-temperature recovery rates would be reduced 50-1000 times. The methyl groups change their mass upon full deuteration from 15 to 18 g/mole and changes in their tunneling dynamics would be easily noticeable (9.5% change in λ and ~50 times change in fixed-

temperature recovery rate for $\lambda_g \approx 20$). The mass of the –OH group changes by 6%, resulting in a 3% change of λ. Results obtained for chlorophyll in water / glycerol environment exclude the possibility of proton / deuteron tunneling affecting spectral dynamics but, taking into account poor quality of this data, could still be consistent with the tunneling involving –OH groups. Could any dynamics observed for Cyt b_6f still originate from the –OH group tunneling in the outside solution? The Cyt b_6f data is of significantly higher quality than the chlorophyll in solution data. It is unlikely that we could miss a 3% change in λ in Cyt b_6f. For instance, if λ were increased by 3%, the recovery of a 30% hole in the deuterated OGP-detergent sample in Figure 5.7 and 5.8 would become slower than what was observed for a 40% hole (short-dashed blue curve in Figure 5.8. As fixed-temperature recovery is preferentially probing the smaller-md^2 tier of the barrier distribution (blue curves in Figure 5.19, dashed blue line in Figure 5.10), one can be confident that this tier belongs to the protein and likely reflects the cooperative dynamics of the hydrogen bond network.

Note that fixed-temperature (5 K) recovery does not directly probe the second, higher-md^2 lower-V component (black curves in Figure 5.19, black dashed line in Figure 5.10), at least within the first 15 hours. Thus, one should be somewhat cautious about claiming its deuteration-independence. However, any deuteration-related effect, if present for this component, cannot possibly be strong, or this component would shift towards the higher λ and would not contribute to the NPHB and hole recovery in the deuterated samples. This would in turn result in a decrease of the apparent NPHB rate for all illumination intensities (second burning channel rendered much slower in competitive burning model, the only channel rendered much slower for some molecules in one-tier-different-md^2 model) and in significant differences in thermocycling (smaller, lower T contribution missing / reduced). These effects were not observed. Given the

location of the chlorophylls within the Cyt b_6f (see Figure 5.1) and the presence of the detergent micelle surrounding the hydrophobic part of the protein in the vicinity of the chlorophylls, chlorophylls inside the protein reporting the dynamics of the –OH groups of the outside environment is not very likely. Presence of a strong detergent effect also suggests that observed dynamics is that of the protein or perhaps protein-in-detergent-micelle rather than that of the outside solvent. Strong quenching of Chl *a* monomer fluorescence in solution and the absence of such strong quenching in protein (the quenching possibly observed in DM-based samples is still two orders of magnitude weaker than quenching in water / glycerol mixture, see Figure 5.18) is still another strong argument against chlorophyll in Cyt b_6f being somehow exposed to the water / glycerol mixture (and exhibiting "glassy" dynamics because of that). The 0.8% difference in λ between protonated and deuterated samples observed in fixed-temperature recovery experiments may be a measure of the imperfections of our experiment or reflect some real minor differences in sample preparation and cooling history. As shown in [68], cooling history may affect how far the pigment-protein systems are from thermal equilibrium and consequently introduce minor variations in the apparent rates of NPHB and of recovery.

5.4.2. Intensity Effect in HGK of the Deuterated Cyt b_6f Samples.

The apparent NPHB rate may be affected by the changes in the balance between spectral hole recovery occurring during the burning (intensity-independent process) and the burning process per se. However, in this scenario one would expect faster burning (as a function of J/cm^2, as in all our HGK figures) for higher intensity. The same photon numbers would be delivered in a

shorter time, which should tilt the balance in favor of burning and against the recovery. Even for 200 $\mu W/cm^2$ (Figure 5.13), we are several orders of magnitude away from the saturating intensities. It was noticed for both CP43 and Cyt b_6f in protonated environment that (all other parameters, such as intensity, being the same) hole burning slows down with the increase of temperature, in agreement with the homogeneous line width increasing with temperature and the peak absorption cross-section decreasing accordingly.[19,20] Similar behavior was observed also for Cyt b_6f in the deuterated environment (Figure 5.5). Thus, slowdown of burning with increasing illumination intensity may be explained by local heating of the immediate protein environment of the chlorophyll molecules by several Kelvin with respect to the "global" temperature of the sample, measured by the macroscopic sensor. For the proposed deuteration-dependent local heating effect to be observable, the bulk thermal conductivity and/or the protein / solvent interface thermal conductance have to be significantly lowered in the case of deuterated solvent. Deuterated substances generally have somewhat lower heat conductivities than their protonated counterparts, thus making some kind of increased local heating more plausible. Comparison of cryogenic-temperature data for protonated and deuterated versions of the same compound appears to be available only for ethanol, and depending on the phase the values are in the range between 0.1 and 1 $W/m \cdot K$.[69] The low-temperature heat conductivity of the deuterated ethanol is indeed somewhat lower than of the regular ethanol. Heat conductivities of either amorphous ice or glycerol at cryogenic temperatures are also in the range of 0.1–1 $W/m \cdot K$.[70,71] The data on various water / cryoprotectant mixtures as well as various tissues is available only down to about 120 K.[72] However, in this temperature range the heat conductivities of the mixtures lay between those of ice and pure glycerol. Similar heat conductivity values were calculated for green fluorescent protein and myoglobin in.[73]

However, careful analysis of a number of steady-state and dynamic scenarios [8] indicates that explaining our results requires several order of magnitude lower bulk heat conductivity values. The remaining possibilities involve higher thermal resistance of the interface between (non-modified, protonated) protein and deuterated outside environment, for instance due to acoustic mismatch. The calculated values of the interface thermal conductance between protein and water are in the 100 MW/($K \cdot m^2$) range at room temperature.[74] The cryogenic-temperature surface heat conductance data is scarce and usually pertains to two solid objects compressed or soldered together. For example, the 90 K 0.2 MPa interface thermal conductance between copper and aluminum nitride is about 300 W/K m^2, with a strong decreasing trend towards lower temperatures.[75] The values necessary to explain our results are on the order of 10 W/Km^2. One should note, however, that for objects that are as small as individual Cyt b_6f dimer, continuum approach to the space inside and outside the protein / amorphous solid interface is not sufficient, and one has to look into exact molecular nature of the relevant vibrations. Vibrations of proteins are quite distinct from those of three-dimensional amorphous materials. Most vibrational modes of harmonic aqueous glass are extended over large volume.[76,77] Most vibrational modes of a harmonic protein, however, are localized to a relatively small region of the protein.[78,79]

Chapter 6

Conclusions and Outlook

6.1 Conclusions

Spectral dynamics of Cyt b_6f manifesting in NPHB experiments is nearly independent of the deuteration of the buffer / glycerol matrix containing the protein (apart from some differences in heat dissipation), and of the detergent employed in the isolation and purification procedure. Apparent differences in NPHB and hole recovery rates between samples with different detergent are attributable to DM-based dimeric Cyt b_6f samples featuring stronger electron-phonon coupling and shorter (and possibly distributed) excited state lifetime, due to quenching by aromatic groups, in agreement with results obtained for DM-based Cyt b_6f samples from other organisms by other groups. Our preliminary results obtained for DM-solubilized Cyt b_6f monomers show behavior that is much more typical for OGP-solubilized dimers than for DM-solubilized dimers. This suggests that DM is not in a direct contact with the Chl *a* but that DM micelle somehow stabilizes the overall structure of the dimer, shifting the chlorophylls and quenching groups with respect to each other and thereby increasing the quenching probability.

Two plausible explanations for spectral dynamics remain. The observed dynamics most likely is the genuine protein dynamics, despite the shape of the barrier distribution(s) resembling $\sim 1/\sqrt{V}$, and likely involves cooperative effects. Alternatively, but less likely one of the two sub-distributions of barriers observed in Cyt b_6f may be due to the outside solvent environment dynamics involving specifically the whole –OH groups. Single proton / deuteron tunneling in the

water / glycerol environment can be safely excluded as the origin of our NPHB observations. The differences in heat dissipation between protonated and deuterated samples are most consistent with the presence of higher interface thermal resistivity between (still protonated) protein and deuterated outside environment, possibly due to phonon or vibration frequency mismatch. Although two-tier burning model presented here adequately describes most observations, it still leaves some questions unanswered. It is possible that our usage of simplified tunneling model based on the WKB approximation is responsible for the remaining discrepancies.

6.2 Future Work

Based on the results and conclusions presented above, the following directions of future work are feasible and some work has already been done along most of the following lines:

- Introducing more advanced treatment of quantum-mechanical tunneling into the NPHB modeling software (collaboration with Sophya Garashchuk, USC). WKB approximation used to derive our relation between the tunneling parameter and the barrier parameters assumes rectangular barriers and scattering particle wavefunctions which are not perfectly justified in the case of the parabolic potential wells.
- Ultra-long experiments (that could be conducted only after purchasing a closed-cycle cryostat) with the aim of exploring fixed-temperature recovery. Are holes clearly recovering well past 50% at 5K?

- Performing similar experiments on different / additional complexes, such as CP29 and LH2 (both characterized by relatively low electron-phonon coupling). This will allow us to further address the issue of variability of the shapes of the barrier (or lambda) distributions and see if the two-component barrier distributions with degenerate range of lambdas are a universal feature of the photosynthetic proteins.
- Experiments on LH2 where some Bchl a were substituted with Chl a molecules. As significant amounts of heat will be introduced into LH2 proteins via exciting the B800 band and subsequent B800-B850 energy transfer, the spectral lines (or holes) belonging to Chl molecules will serve as local thermometers.

References

[1] *Allen, James P*. Biophysical chemistry p150-151 ; 572′.43—dc22 2007038528 ISBN: 978-1-4051-2436-2 **2008**

[2]*Unnati Ahluwalia# , Nidhi Katyal# and Shashank Deep** MODELS OF PROTEIN FOLDING Department of Chemistry, Indian Institute of Technology, New Delhi 110016, India #

[3] *H.P. Trommsdorff, A. Corval, and L. von Laue* Spectral hole burning: Spontaneous and photoinduced tunneling reactions in low temperature solids Laboratoire de Spectrom6trie Physique, associd au C.N.R S. Universite Joseph Fourier, Grenoble I - BP. 87,38402 St. Martin d'Heres, France

[4] *DMITRIY SHEVELA, LARS OLOF BJO¨RN, GOVINDJEE* Oxygenic Photosynthesis Oxygenic Photosynthesis Natural and Artificial Photosynthesis: Solar Power as an Energy Source edited By Reza Razeghifard **2013**

[5] *Herbert van Amerongen, Leonas Valkunas, Rienk van Grondelle* Photosynthetic excitons. Chapter1. Organization, spectral properties and excitation energy transfer in photosynthesis.**2000**

[6] *R. Jankowiak, J. M. Hayes, and G. J. Small** Spectral Hole-Burning Spectroscopy in Amorphous Molecular Solids and Proteins Department of Chemistry and Ames Laboratory— USDOE, Iowa State University, Ames, Iowa 50011

[7] *W. E. Moerner* Topics in current physics Volume 44 Persistent Spectral Hole-Burning: Science and Applications

[8] *Golia Shafiei* Protein Dynamics in Cytochrome b6f Explored by Spectral Hole Burning. **March 2016**

[9*] R. Jankowiak and G. J. Small,* \Hole-burning spectroscopy and relaxation dynamics of amorphous solids at low temperatures.," Science (New York, N.Y.), vol. 237, pp. 618{25, aug 1987.

[10] *Reddy, N. R. S.; Lyle, P. A.; Small, G. J.* Photosynth. Res. 1992, 31,167.

[11] Detection of ultrasound-modulated diffuse photons using spectral-hole burning. Youzhi Li,1 Philip Hemmer,2 Chulhong Kim,1 Huiliang Zhang,2 and Lihong V. Wang1,*

[12] . *Seyed Mahdi Najafi Shooshtari* Modeling and Characterization of Protein Energy Landscape at Low Temperature using Spectral Hole Burning Spectroscopy. A Thesis in The Department of Physics Concordia University 2013

[13] *Zaida Luthey-Schulten and Peter G. Wolynes* THEORY OF PROTEIN FOLDING: The Energy Landscape Perspective Jose Nelson Onuchic ´ Department of Physics, University of California at San Diego, La Jolla, California 92093-0319 School of Chemical Sciences, University of Illinois, Urbana, Illinois 61801 *Annu. Rev. Phys. Chem. 1997. 48:545–600 Copyright c 1997 by Annual Reviews Inc.*

[14] *PETER E. LEOPOLD*t, MAURICIO MONTAL*t, AND Jost NELSON ONUCHIC*§*Protein folding funnels: A kinetic approach to the sequence-structure relationship Proc. Nati. Acad. Sci. USA Vol. 89, pp. 8721-8725, September 1992 Biophysics

[15] *Peter G. Wolynes and Zan Luthey-Schulten* The Energy Landscape Theory of Protein Folding. School of Chemical Sciences, University of Illinois, Urbana, Illinois 61801

[16] *J. N. ONUCHIC, P. G. WOLYNESt, Z. LUTHEY-SCHULTENt, AND N. D. SoccI Proc.* Biophysics Toward an outline of the topography of a realistic proteinfolding funnel Natl. Acad. Sci. USA Vol. 92, pp. 3626-3630, April 1995

[17] *K. S. Gilroy &W. A. Phillips* An asymmetric double-well potential model for structural relaxation processes in amorphous materials.

[18] *Clemens M¨uller,1, ∗Jared H. Cole,2, † and J¨urgen Lisenfeld3, ‡*Towards understanding two-level-systems in amorphous solids - Insights from quantum devices

[19] *Najafi, M.; Herascu, N.; Seibert, M.; Picorel, R.; Jankowiak, R.; Zazubovich, V*. Spectral Hole Burning, Recovery, and Thermocycling in Chlorophyll−Protein Complexes: Distributions of Barriers on the Protein Energy Landscape, *J. Phys. Chem.* B **2012**, *116*, 11780-11790.

[20] *Najafi, M.; Herascu, N.; Shafiei, G.; Picorel, R.; Zazubovich, V.* Conformational Changes in Pigment-Protein Complexes at Low Temperatures – Spectral Memory and a Possibility of Cooperative Effects, *J. Phys. Chem. B* **2015**, *119*, 6930−6940.

[21] *María A. Luján, Patricia Lorente, Valter Zazubovich & Rafael Picorel* A simple and efficient method to prepare pure dimers and monomers of the cytochrome b 6 f complex from spinach.

[22] *H. Maier, B. M. Kharlamov, and D. Haarer* Investigation of Tunneling Dynamics by Optical Hole-Burning Spectroscopy Tumeling systems in amorphous and crystalline solids *1* Pablo Esquinazi, (ed.) p. cm*. ISBN 978-3-642-08371-6 ISBN 978-3-662-03695-2 (eBook) DOI 10.1007/978-3-662-03695-2*

[23*] S. P. Love and A. J. Sievers,* "Persistent infrared spectral hole burning of the sulfur—hydrogen vibrational mode in hydrogenated As2S3 glass," *Chem. Phys. Lett.*, vol. 153, no. 5, pp. 379–384, Dec. 1988.

[24] *Alexey Amunts,‡ J€org Pieper,§,3 Klaus-Dieter Irrgang,|| Rafael Picorel,^ Michael Seibert,# and Valter Zazubovich*,†* Parameters of the Protein Energy Landscapes of Several Light-Harvesting Complexes Probed via Spectral Hole Growth Kinetics Measurements Nicoleta Herascu,† Mehdi Najafi,†

[25*] J. Pieper and A. Freiberg,* The Biophysics of Photosynthesis, Edited by John Golbeck and Art van der Est, ch. Electron{Phonon and Exciton{Phonon Coupling in Light Harvesting, Insights from Line-Narrowing Spectroscopies, pp. 45{77. New York, NY: Springer New York, 2014.

[26] *W. Yen and R. Brundage*, \Fluorescence line narrowing in inorganic glasses: linewidth measurements," Journal of luminescence, vol. 36, no. 4, pp. 209{220, 1987

[27] *M. Reppert, V. Naibo, and R. Jankowiak,* \Accurate modeling of fluorescence line narrowing difference spectra: Direct measurement of the single-site fluorescence spectrum," Journal of Chemical Physics, vol. 133, no. 1, 2010.

[28] *O. Sild and K. Haller* Zero-Phonon Lines and Spectral Hole Burning in Spectroscopy and Photochemistry (Springer-Verlag, Berlin, 1988).

[29] *M. Belen Oviedo and Cristian G. Sanchez** Transition Dipole Moments of the Qy Band in Photosynthetic Pigments

[30] Agostiano, A.; Della Monica, M.; Palazzo G.; Trotta, M. Chlorophyll a Autoaggregation in Water Rich Region, Biophys. Chem. **1993,** 47, 193–202

[31] *Vladkova, R.* Chlorophyll *a* Self-assembly in Polar Solvent–Water Mixtures, *Photochem. Photobiol*. **2000**, *71*, 71–83.

[32] *Byrdin, M.; Jordan, P.; Krauß, N.; Fromme, P.; Stehlik, D.; Schlodder, E.* Light Harvesting in Photosystem I: Modeling Based on the 2.5-Å Structure of Photosystem I from *Synechococcus elongatus*, *Biophys. J*. **2002**, *83*, 433–457.

[33] *Mike Reppert, Virginia Naibo, Ryszard Jankowiak* Accurate modeling of fluorescence line narrowing difference spectra: Direct measurement of the single-site fluorescence spectrum. The Journal of Chemical Physics **133**, 014506 (2010)

[34] *Arthur C.Ley David C.Mauzerall* Excitation Wavelength-Dependent Electron−Phonon and Electron−Vibrational Coupling in the CP29 Antenna Complex of Green Plants Margus Rätsep, Jörg Pieper, Klaus-Dieter Irrgang, Arvi Freiberg

[35] Absolute absorption cross-sections for Photosystem II and the minimum quantum requirement for photosynthesis in Chlorella vulgaris.

[36] *T. Reinot and G. J. Small* Modeling of dispersive nonphotochemical hole growth kinetics data: Alphthalocyanine tetrasulphonate in hyperquenched glassy water," Journal of Chemical Physics, vol. 113, no. 22, pp. 10207{10214, 2000.

[37] *J. Pieper and A. Freiberg,* The Biophysics of Photosynthesis, Edited by John Golbeck and Art van der Est, ch. Electron{Phonon and Exciton{Phonon Coupling in Light Harvesting, Insights from Line-Narrowing Spectroscopies, pp. 45{77. New York, NY: Springer New York, 2014.

[38] *W. Yen and R. Brundage*, \Fluorescence line narrowing in inorganic glasses: linewidth measurements," Journal of luminescence, vol. 36, no. 4, pp. 209{220, 1987.

[39]*M. Reppert, V. Naibo, and R. Jankowiak,* \Accurate modeling of fuorescence line narrowing difference spectra: Direct measurement of the single-site uorescence spectrum," Journal of Chemical Physics, vol. 133, no. 1, 2010.

[40]*M. R□atsep, J. Pieper, K. D. Irrgang, and A. Freiberg,* \Excitation wavelength-dependent electron-phonon and electron-vibrational coupling in the CP29 antenna complex of green plants," Journal of Physical Chemistry B, vol. 112, no. 1, pp. 110{118, 2008

[41]*H. Frauenfelder, S. Sligar, and P. Wolynes,* \The energy landscapes and motions of proteins," 1991.

[42] *P. W. Fenimore, H. Frauenfelder, B. H. McMahon, and R. D. Young*, \Proteins are paradigms of stochastic complexity," Physica A: Statistical Mechanics and its Applications, vol. 351, no. 1, pp. 1{13, 2005.

[43] *C. Hofmann, T. J. Aartsma, H. Michel, and J. K□hler*, \Direct observation of tiers in the energy landscape of a chromoprotein: a single-molecule study.," Proceedings of the National Academy of Sciences of the United States of America, vol. 100, no. 26, pp. 15534{15538, 2003

[44] *Jankowiak, R.; Hayes, J. M.; Small, G. J*. Spectral Hole-Burning Spectroscopy in Amorphous Molecular Solids and Proteins, *Chem. Rev.* 1993*, 93*, 1471-1502.

[45] *Reinot, T.; Dang, N. C.; Small, G. J.* A Model for Persistent Hole Burned Spectra and Hole Growth Kinetics that Includes Photoproduct Absorption: Application to Free Base Phthalocyanine in Hyperquenched Glassy Ortho-dichlorobenzene at 5 K. *J. Chem. Phys*. 2003, *119*, 10404–10414.

[46]*Reinot, T.; Small, G. J.* Modeling of Dispersive Nonphotochemical Hole Growth Kinetics Data. Al-phthalocyanine Tetrasulphonate in Hyperquenched Glassy Water, *J. Chem. Phys.* 2000, *113*, 10207–10214.

[47] *Reinot, T.; Hayes, J. M.; Small, G. J.* Laser-induced Hole Filling and Spectral Diffusion of Aluminum Phthalocyanine Tetrasulfonate in Hyperquenched Glassy Films, *J. Chem. Phys.* 1999, *110*, 4820-4827.

[48] *Grozdanov, D.; Herascu, N.; Reinot, T.; Jankowiak, R.; Zazubovich,* V. Low-Temperature Protein Dynamics of the B800 Molecules in the LH2 Light-Harvesting Complex: Spectral Hole Burning Study and Comparison with Single Photosynthetic Complex Spectroscopy, *J. Phys. Chem.* B 2010, *114*, 3426-3438.

[49] *Love, S. P.; Mungan, C. E.; Sievers A. J.; Campbell, J. A.* Persistent Infrared Spectral Hole Burning of Tb^{3+} in the Glasslike Mixed Crystal $Ba_{1-X-Y}La_xTb_yF_{2+x+y}$, *J. Opt. Soc. Am.* B 1992, *9*, 794-799.

[50] *Dang, N. C.; Reinot, T.; Reppert, M.; Jankowiak, R.* Temperature Dependence of Hole Growth Kinetics in Aluminum−Phthalocyanine−Tetrasulfonate in Hyperquenched Glassy Water, *J. Phys. Chem. B*, 2007, 111, 1582-1589

[51] *Kim, W.-H.; Reinot, T.; Hayes, J.M.; Small, G.J.* Nonphotochemical Hole Burning in Hyperquenched Glassy Films of Water: A Pronounced Deuteration Effect. *J. Chem. Phys.* 1996**,** *104*, 6415-6417.

[52] *Monks-Corrigan, T.; Riesen, H.* Host Deuteration Effects in Non-Photochemical Spectral Hole-burning in the R_1-line of $[Cr(oxalate)_3]^{3-}$ in Ethylene Glycol/water. *Chem. Phys. Lett.* 2006**,** 4*19,* 321–325.

[53] *Köhler, W.; Friedrich, J.* Distribution of Barrier Heights in Amorphous Organic Materials, *Phys. Rev. Lett.* 1987, *59*, 2199-2202.

[54] *Köhler, W.; Meiler, J.; Friedrich, J*. Tunneling Dynamics of Doped Organic Low-temperature Glasses as Probed by a Photophysical Hole-burning System, *Phys. Rev* B 1987, *35,* 4031-4037.

[55] *Köhler, W., Friedrich, W., Scheer, H.,* Conformational Barriers in Low-temperature Proteins and Glasses. *Phys. Rev*. A 1988, *37*, 660–662.

[56] *den Hartog, F. T. H.; van Papendrecht, C.; Störkel, U.; Völker, S.* Protein Dynamics in Photosystem II Complexes of Green Plants Studied by Time-Resolved Hole-Burning. *J. Phys. Chem. B* **1999,** *103,* 1375-1380.

[57] *Anderson, P. W.; Halperin, B. I.; Varma, C. M.* Anomalous Low-temperature Thermal Properties of Glasses and Spin Glasses. *Phil. Mag*., 1972, *25*, 1-9.

[58] *Phillips, W. A.,* Tunneling States in Amorphous Solids. *J. Low. Temp. Phys*. 1972, *7*, 351 360.

[59] *Riesen, H.; Hughes, J. L.* Massive Enhancement of Persistent Spectral Hole-Burning in the R-Lines of $NaMgAl(oxalate)_3 \cdot 9H2O:Cr(III)$ by Partial Deuteration. *Chem. Phys. Lett.* 2003**,** *372*, 563–568.

[60] *Adolphs, J.; Berrer, M.; Renger, T.* Hole-Burning Spectroscopy on Excitonically Coupled Pigments in Proteins: Theory Meets Experiment. *J. Am. Chem. Soc.* 2016, *138*, 2993–3001.

[61] *Oikawa, H.; Fujiyoshi, S.; Dewa, T.; Nango, M. Matsushita, M.* How Deep is the Potential Well Confining a Protein in a Specific Conformation? A Single-molecule Study on Temperature Dependence of Conformational Change between 5 and 18 K. *J. Am. Chem. Soc.* 2008, *130*, 4580−4581.

[62] *Baniulis, D.; Zhang, H.; Zakharova, T.; Hassan, S. S.; Cramer, W. A.* Purification and Crystallization of the Cyanobacterial Cytochrome b6 f Complex. In Methods in Molecular Biology, Vol. 684, Photosynthesis Research Protocols; Carpentier, R., Ed.; Springer: New York, 2011; pp 65−77.

[63] *Pierre, Y.; Breyton, C.; Kramer, D.; Popot, J. L.* Purification and Characterization of the Cytochrome b6f Complex from Chlamydomonas reinhardtii. J. Biol. Chem. 1995, 270, 29342−29349.

[64] *Lujan, M.A.; Lorente, P.; Zazubovich, V.; Picorel, R*. A simple and efficient method to prepare pure dimers and monomers of the cytochrome b_6f complex from spinach. *Photosynth. Res.* **2017**, *132*, 305-305.

[65] *Hughes, J. L.; Krausz, E.; Smith, P. J.; Pace, R. J.; Riesen, H.* Probing the Lowest Energy Chlorophyll a States of Photosystem II via Selective Spectroscopy: New Insights on P680. *Photosynth Res.* **2005,** *84*, 93-98.

[66] *Hughes, J. L.; Picorel, R.; Seibert, M.; Krausz, E.* Photophysical Behavior and Assignment of the Low-Energy Chlorophyll States in the CP43 Proximal Antenna Protein of Higher Plant Photosystem II. *Biochemistry* **2006**, *45,* 12345-12357.

[67] *Hughes, J. L.; Prince, B. J.; Peterson Årsköld, S.; Krausz, E.; Pace, R. J.; Picorel, R.; Seibert, M.* Photo-Conversion of Chlorophylls in Higher-Plant CP43 Characterized by Persistent Spectral Hole Burning at 1.7K. *J. Lumin*. **2004**, *108*, 131–136.

[68] *Najafi, M.; Zazubovich, V.* Monte-Carlo Modeling of Spectral Diffusion Employing Multi-well Protein Energy Landscapes: Application to Pigment-Protein Complexes Involved in Photosynthesis. *J. Phys. Chem. B* **2015**, *119*, 7911-7921.

[69] Krivchikov, A. I.; Bermejo, F. J.; Sharapova, I. V.; Korolyuk, O. A.; Romantsova, O. O. Deuteration Effects in the Thermal Conductivity of Molecular Glasses. Low Temp. Phys. **2011**, 37, 517-523.

[70]*Talon, C.; Zou, Q. W.; Ramos, M. A.; Villar, R.; Vieira, S.* Low-Temperature Specific Heat and Thermal Conductivity of Glycerol**.** *Phys. Rev. B* **2001,** 65, 012203.

[71]Ahmad, N. Thermal Conductivity of Ice. Phys. Status Solidi B **1994**, 181, 37-44.

[72]*Choi, J.; Bischof, J. C.* Review of Biomaterial Thermal Property Measurements in the Cryogenic Regime and Their Use for Prediction of Equilibrium and Non-Equilibrium Freezing Applications in Cryobiology. *Cryobiology,* 2010, *60*, 52–70.

[73]*Yu. X.; Leitner, D. M.* Heat Flow in Proteins: Computation of Thermal Transport Coefficients. *J. Chem. Phys.* **2005**, *122*, 054902.

[74]Lervik, A.; Bresme, F.; Kjelstrup, S.; Bedeaux, D.; Rubi, J. M. Heat Transfer in Protein–Water Interfaces. Phys. Chem. Chem. Phys. **2010**, 12, 1610–1617.

[75]*Shi, L.; Wu, G.; Wang, H.-L.; Yu, X.-M*. Interfacial Thermal Contact Resistance between Aluminum Nitride and Copper at Cryogenic Temperature. *Heat Mass Transfer* **2012**, *48*, 999-1004,

[76]*Pohorille, A.; Pratt, L. R.; LaViolette, R. A.; Wilson, M. A.; MacElroy, R. D.* Comparison of the Structure of Harmonic Aqueous Glasses and Liquid Water. *J. Chem. Phys.* **1988**, *87*, 6070-6077;

[77]Cho, M.; Fleming, G. R.; Saito, S.; Ohmine, I.; Stratt, R. M. Instantaneous Normal Mode Analysis of Liquid Water. J. Chem. Phys. **1994**, 100, 6672-6683;

[78]*Go, N.; Noguti, T.; Nishikawa, T*. Dynamics of a Small Globular Protein in Terms of Low-Frequency Vibrational Modes. *Proc. Natl. Acad. Sci. U. S. A.* **1983**, *80*, 3696-3700.

[79]*Brooks, B. R.; Karplus, M.* Harmonic Dynamics of Proteins: Normal Modes and Fluctuations in Bovine Pancreatic Trypsin Inhibitor. *Proc. Natl. Acad. Sci. U. S. A.* **1983**, *80*, 6571-6575.

[80]Peterman, E. J.; Wenk, S.-O.; Pullerits, T.; Pålsson, L.-O.; van Grondelle, R.; Dekker, J. P.; Rogner, M.; van Amerongen, H. Fluorescence and Absorption Spectroscopy of the Weakly Fluorescent Chlorophyll a in Cytochrome b_6f of Synechocystis PCC6803. Biophys. J. **1998**, 75, 389–398.

[81]*Dashdorj, N.; Zhang, H.; Kim, H.; Yan, J.; Cramer, W. A.; Savikhin, S.* The Single Chlorophyll *a* Molecule in the Cytochrome b_6f Complex: Unusual Optical Properties Protect the Complex against Singlet Oxygen. *Biophys. J.* **2005**, *88*, 4178–4187.

[82]*Yan, J.; Dashdorj, N.; Baniulis, D.; Yamashita, E.; Savikhin, S.; Cramer, W. A.* On the Structural Role of the Aromatic Residue Environment of the Chlorophyll *a* in the Cytochrome b_6f Complex. *Biochemistry* **2008,** *47,* 3654–3661.

[83]*Herascu, N.; Ahmouda, S.; Picorel, R.; Seibert¸ M.; Jankowiak, R.; Zazubovich, V.* Effects of the Distributions of Energy or Charge Transfer Rates on Spectral Hole Burning in Pigment-Protein Complexes at Low Temperatures. *J. Phys. Chem. B* **2011**, *115*, 15098-15109.

[84]*Whitelegge JP, Zhang H, Aguilera R, Taylor RM, Cramer WA*. "Full subunit coverage liquid chromatography electrospray ionization mass spectrometry (LCMS+) of an oligomeric membrane protein: cytochrome b(6)f complex from spinach and the cyanobacterium *Mastigocladus laminosus*". *Molecular & Cellular Proteomics*. **1** (10): 816–27. **Oct 2002**

[85] *D. Shevela, Photosynthetic* Water Oxidation. Role of Inorganic Cofactors and Species Differences, VDM Verlag Dr. M¨uller, Saarbr¨ucken, 2008.

[86] *A.J.Nair*. Principles of Biotechnology and Genetic Engineering Second Edition p.138 **2010**

[87] Plants in Action 1.2.2 - Chlorophyll absorption and photosynthetic action spectra Australian Society of Plant Scientists, New Zealand Society of Plant Biologists, and New Zealand Institute of Agricultural and Horticultural Science **2010–2018** http://plantsinaction.science.uq.edu.au/

[88] *J. H. Golbeck* (Ed.), Photosystem I. The Light-Driven Plastocyanin:Ferredoxin Oxidoreductase, Springer, Dordrecht, 2006

[89]. *P. Fromme, P. Jordan, N. Krauß,* Structure of photosystem I, Biochim. Biophys. Acta 1507 (2001) 5–31.

[90]. *P. Fromme, I. Grotjohann*, Structural analysis of cyanobacterial photosystem I. In: J. H. Golbeck (Ed.), *Photosystem I. The Light-Driven Plastocyanin:Ferredoxin Oxidoreductase*, Springer, Dordrecht, 2006, pp. 47–69.

[91] *G. Tomita and E. Rabinowitch,* \Excitation energy transfer between pigments in photosynthetic cells.," Biophysical journal, vol. 2, no. 6, pp. 483{499, **1962.**

[92*] R. Croce and H. van Amerongen*, \Natural strategies for photosynthetic light harvesting,"Nature Chemical Biology, vol. 10, no. 7, pp. 492{501, 2014.

[93] *E. Yamashita, H. Zhang, and W. A. Cramer*, \Structure of the Cytochrome b6f Complex: Quinone Analogue Inhibitors as Ligands of Heme cn," Journal of Molecular Biology, vol. 370, no. 1, pp. 39{52, **2007.**

[94] *Rabinowitch and Govindjee,* Excitation Energy Transfer and Energy Migration **1969**, Photosynthesis, John Wiley & Sons edited by Govindjee
http://www.life.illinois.edu/govindjee/biochem494/foerster.htm

[95] *J. Friedrich*, Biochemical Spectroscopy, vol. 246 of Methods in Enzymology. Elsevier, **1995**

[96] *H. Frauenfelder, F. Parak, and R. D. Young,* \Conformational substates in proteins.," Annual review of biophysics and biophysical chemistry, vol. 17, pp. 451{479, 1988.

[97] *R. H. Austin, K. W. Beeson, L. Eisenstein, H. Frauenfelder, and I. C. Gunsalus*, \Dynamics of ligand binding to myoglobin.," Biochemistry, vol. 14, no. 24, pp. 5355{5373, 1975.

[98] *Clemens Muller, Jared H. Cole,2, ,Jurgen Lisenfeld,* Towards understanding two-level-systems in amorphous solids - Insights from quantum devices. **May 4, 2017**

[99] *Leopold PE[1], Montal M, Onuchic JN* Protein folding funnels: a kinetic approach to the sequence-structure relationship. Department of Physics, University of California, San Diego, La Jolla 92093-0319. **1992 Sep 15**;89(18):8721-5.

[100] Principles of Cell Biology (BIOL2060) Department of Biology Memorial University of Newfoundland http://www.mun.ca/biology/desmid/brian/BIOL2060/BIOL2060-11/CB11.html

[101] An Overview of Photosynthesis. BioCoach Activity http://www.phschool.com/science/biology_place/biocoach/photosynth/overview.html

[102] Photosynthetic microorganisms, Range of absorptions. http://ysleo.blogspot.ca/2008/05/

[103] Thermodynamics and Photosynthesis http://eesc.columbia.edu/courses/ees/slides/life/chlorophyll_a_b.gif

[104] Franck–Condon principle, Wikipedia, the free encyclopedia. https://en.wikipedia.org/wiki/Franck%E2%80%93Condon_principle